

This is an Open Access document downloaded from ORCA, Cardiff University's institutional repository: <https://orca.cardiff.ac.uk/id/eprint/159137/>

This is the author's version of a work that was submitted to / accepted for publication.

Citation for final published version:

Zhou, Wenxiao, Chang, Feng, Huang, Bo, Xia, Bin, Fu, Dong, Chi Fru, Ernest, Li, Haiquan, Lu, Xinbiao and Mao, Cheng 2024. Oceanic subduction to continental collision in the NE Proto-Tethys revealed by early Paleozoic eclogites with high-temperature granulite-facies overprinting in the East Kunlun orogenic belt, northern Tibet. *GSA Bulletin* 136 (1-2), pp. 619-636. 10.1130/B36718.1

Publishers page: <https://doi.org/10.1130/B36718.1>

Please note:

Changes made as a result of publishing processes such as copy-editing, formatting and page numbers may not be reflected in this version. For the definitive version of this publication, please refer to the published source. You are advised to consult the publisher's version if you wish to cite this paper.

This version is being made available in accordance with publisher policies. See <http://orca.cf.ac.uk/policies.html> for usage policies. Copyright and moral rights for publications made available in ORCA are retained by the copyright holders.



1 Oceanic subduction to continental collision in the NE Proto-  
2 Tethys revealed by Early Paleozoic eclogites with high-T granulite  
3 facies overprinting in the East Kunlun orogenic belt, northern  
4 Tibet

5  
6 **Wenxiao Zhou<sup>1\*</sup>, Feng Chang<sup>2</sup>, Bo Huang<sup>3,4</sup>, Bin Xia<sup>5\*</sup>, Dong Fu<sup>4,6</sup>, Ernest Chi Fru<sup>7</sup>, Haiquan  
7 Li<sup>1</sup>, Xinbiao Lü<sup>8</sup>, Cheng Mao<sup>8</sup>**

8  
9 *<sup>1</sup>Institute of Geological Survey, China University of Geosciences, Wuhan 430074, China*

10 *<sup>2</sup>School of Earth and Space Sciences, Peking University, Beijing 100871, China*

11 *<sup>3</sup>Badong National Research and Observation Station for Geohazards, China University of Geosciences,  
12 Wuhan 430074, China*

13 *<sup>4</sup>Central for Global Tectonics, School of Earth Sciences, China University of Geosciences, Wuhan 430074,  
14 China*

15 *<sup>5</sup>School of Earth Sciences, China University of Geosciences, Wuhan 430074, China*

16 *<sup>6</sup>State Key Laboratory of Geological Processes and Mineral Resources, China University of Geosciences,  
17 Wuhan 430074, China*

18 *<sup>7</sup> School of Earth and Environmental Sciences, Centre for Geobiology and Geochemistry, Cardiff University,  
19 Cardiff CF10 3AT, Wales, the United Kingdom*

20 *<sup>8</sup> School of Earth Resources, China University of Geosciences, Wuhan 430074, China*

21

22 \* Corresponding authors: [zhouwenxiao@cug.edu.cn](mailto:zhouwenxiao@cug.edu.cn) (W.X. Zhou); [xiabin@cug.edu.cn](mailto:xiabin@cug.edu.cn) (B. Xia)

23 **ABSTRACT**

24 The East Kunlun orogenic belt (EKOB) in the northern Tibetan Plateau records a long-term  
25 accretionary and collisional history in the northeastern Proto-Tethys Ocean, important for  
26 reconstructing the paleogeography of Early Paleozoic East Asia. Here we present an integrated  
27 petrology, geochemistry, geochronology, and metamorphic  $P$ – $T$  study of newly found eclogites in  
28 the middle Nuomuhong segment of the EKOB. The eclogites are composed mainly of garnet,  
29 omphacite and low sodium clinopyroxene, amphibole and plagioclase with minor orthopyroxene,  
30 biotite, quartz, accessory rutile, ilmenite, titanite and zircon. Detailed petrographic observations,  
31 conventional geothermobarometry and phase equilibrium modeling, point to the presence of five  
32 metamorphic mineral assemblages with corresponding  $P$ – $T$  conditions related to: (1) prograde  $M_1$   
33 stage  $P$ – $T$  estimates  $>14.0$  kbar/ $\sim 470$ – $506$  °C; (2)  $P_{max}$   $M_2$  eclogite facies stage  $P$ – $T$  conditions of  
34  $\sim 26$  kbar/ $\sim 570$ °C; (3) early retrograde  $M_3$  high- $P$  granulite facies stage; (4) subsequent  $M_4$   
35 retrograde medium- $P$  granulite facies at  $T_{max}$  of  $\sim 860$ – $900$ °C; and (5) later  $M_5$  retrograde  
36 amphibolite facies stage  $P$ – $T$  conditions of  $<6.2$  kbar/ $\sim 710$ – $730$ °C. These  $P$ – $T$  estimates define a  
37 clockwise  $P$ – $T$  path characterized by heating during the  $P_{max}$  formation of the eclogite facies, to the  
38  $T_{max}$  exhumation stage for the granulite lithologies, the latter of which is identified for the first time  
39 in retrograde eclogites from the EKOB. Whole-rock geochemical composition indicate a mid-  
40 oceanic ridge basalt (MORB) affinity for the eclogites protoliths and a fragmented oceanic crust  
41 origin. SHRIMP zircon U–Pb isotopic analyses for the eclogite yielded two groups of weighted  
42 mean  $^{206}\text{U}/^{238}\text{Pb}$  ages of  $464\pm 8$  Ma and  $419\pm 4$  Ma, interpreted as the ages of the eclogite protolith  
43 and the lower threshold for peak eclogite facies metamorphism, respectively. Our new data, together  
44 with regional eclogite facies metamorphism, suggest a ca. 520–460 Ma age for the subduction of

45 the eastern Kunlun oceanic crust, within the northern Proto-Tethys Ocean, to a depth of ~83 km, with  
46 early subduction–accretionary orogenesis occurring at ca. 419 Ma. Overprinting by high-*T* granulite  
47 facies, linked to the maturation of the collisional orogenesis, point to exhumation of the middle to  
48 shallow oceanic crust at this time. Collectively, the preserved eclogite and high-temperature (*T*)  
49 granulite mineral assemblage provide new constraints on the tectonic evolution and detailed  
50 accretionary-to-collisional orogenesis of the Proto-Tethys Ocean. They suggest that the ca. 428–411  
51 Ma subduction-collisional event marked the termination of the Proto-Tethys Ocean and the eventual  
52 formation of a ~500-km-long, high to ultra-high pressure metamorphic belt in the EKOB.

53

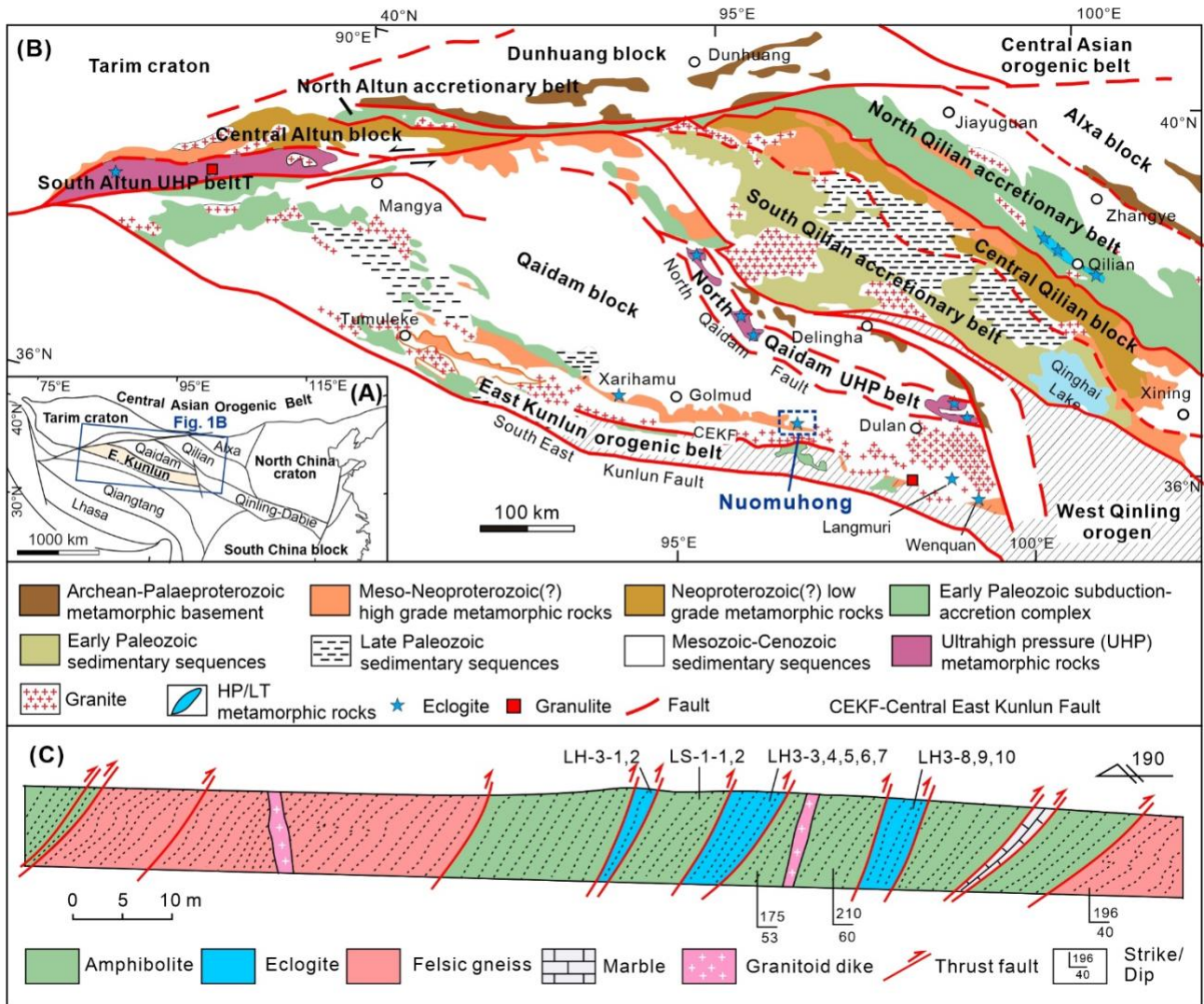
54 **Keywords:** eclogite; subduction; continental collision; Proto-Tethys Ocean; East Kunlun; northern  
55 Tibet

## 56 INTRODUCTION

57 Eclogite is a dense high pressure (HP) to ultra-high pressure (UHP) metamorphic rock  
58 comprised dominantly of omphacite and garnet, commonly associated with suture zones of  
59 accretionary and collisional orogenic belts (Bingen et al., 2001; Dobretsov, 1991; Hertgen et al.,  
60 2016; Klonowska et al., 2016; Meng et al., 2016; Sajeev et al., 2013; Schorn and Diener, 2017;  
61 Smith, 1984; Sobolev et al., 1986). Some eclogites may undergo high temperature (HT) and even  
62 ultra-high temperature (UHT) metamorphic overprinting during collisional orogenesis (Wang et al.,  
63 2022a; Wang et al., 2021). The reconstruction of the pressure–temperature–time ( $P$ – $T$ – $t$ ) path for  
64 eclogite, reliant on proper estimates of pressure–temperature ( $P$ – $T$ ) evolution and determination of  
65 precise metamorphic ages, is thus important for deciphering the thermal history and large-scale  
66 tecto-orogenic processes along paleo-subduction-collision interfaces (Hertgen et al., 2016; Wang et  
67 al., 2017).

68 The Tethyan orogenic system, comprised of the Proto-Tethys, Paleo-Tethys to the Neo-Tethys,  
69 is the largest collisional orogen on Earth (Dong et al., 2018; Şengör, 1984; Zhao et al., 2018). Its  
70 reconstruction represents one of the most important and yet difficult to resolve puzzles in solid earth  
71 science research. In northern Tibet, northwest China, two early Paleozoic HP/UHP metamorphic  
72 belts exist (Fig. 1). The succession includes a HP metamorphic belt in the North Qilian orogenic  
73 belt and a UHP metamorphic belt in the northern Qaidam block, with interpreted formation in  
74 oceanic and continental subduction zone environments, respectively, during the evolution of the  
75 Proto-Tethyan orogenic belts (Han et al., 2015; Song et al., 2018a; Song et al., 2014; Song et al.,  
76 2012; Song et al., 2007; Yu et al., 2013a; Zhang et al., 2010a; Zhang et al., 2016; Zhang et al.,  
77 2015a; Zhang et al., 2008; Zhang et al., 2009; Zhang et al., 2015b). Recently, a several-kilometer-

78 wide HP/UHP metamorphic belt was recognized along the Central East Kunlun Fault in the East  
79 Kunlun orogenic belt (EKOB, Fig. 1) (Chen et al., 2016; Meng et al., 2015a; Qi et al., 2014; Qi et  
80 al., 2016a; Song et al., 2018b). This metamorphic belt was regarded as a subduction-collision suture  
81 zone that records the tectonic evolution of the eastern Kunlun Ocean-a branch in the Proto-Tethys  
82 Ocean (Bi et al., 2022; Song et al., 2018b). despite decades of igneous and metamorphic research,  
83 the tectonic affinity of eclogite protoliths, the mechanism for subduction and exhumation, the  
84 details of orogenesis in the EKOB and the evolution of the Proto-Tethys Ocean remain controversial  
85 (Dong et al., 2018; Feng et al., 2023; Sun et al., 2022; Wang et al., 2022b; Yu et al., 2020a). Some  
86 researchers suggested that the late Ordovician Tumuleke glaucophane schist and associated gabbro  
87 ( $^{40}\text{Ar}/^{39}\text{Ar}$  age:  $445 \pm 2$  Ma) may signify the termination of oceanic subduction and the beginning of  
88 continental collision in late Ordovician (Mo et al., 2007), whereas others proposed that the final  
89 closure of the ocean basin occurred in mid-Silurian (Lu et al., 2010). New data suggest two  
90 discontinuous and distinct orogenic cycles from the Proto-Tethys to the Paleo-Tethys in the EKOB  
91 (Feng et al., 2023).



92  
 93 **Figure 1.** (A) Tectonic sketch map showing the major cratons and orogenic belts in northern China (Fu et al.,  
 94 2022a) . (B) Simplified geological map showing tectonic units in the northern Tibetan Plateau (modified after  
 95 (Meng et al., 2017; Zhang et al., 2015b; Zhang et al., 2017)). The locations of eclogites in the Nuomuhong  
 96 area and other segments of the EQOB are marked (Meng et al., 2013b; Qi et al., 2014; Qi et al., 2016a; Song  
 97 et al., 2018b). (C) An approximately N-S structural cross-section of the Nuomuhong area showing the main  
 98 rock types and the location of samples.

99  
 100 In this contribution, we report a newly found eclogite that was overprinted by high-*T* granulite  
 101 facies metamorphism in the Nuomuhong region in the middle segment of the EKOB (Figs. 1B and

102 1C). We present an integrated study combining petrology, whole-rock geochemistry, and SHRIMP  
103 zircon U–Pb ages from the eclogite to constrain its protolith and metamorphic  $P$ – $T$ – $t$  evolution,  
104 linked to two-stage ocean crust subduction and continental collision in the northeastern Proto-  
105 Tethys domain. The new metamorphic evidence together with regional geological data in the EKOB,  
106 highlight the early Paleozoic accretionary history and collisional orogenesis of the Proto-Tethyan  
107 EKOB.

108

## 109 **GEOLOGICAL SETTING AND SAMPLING**

110 The East Kunlun orogenic belt (EKOB) in the northern Tibet Plateau is bounded by the Qaidam  
111 block in the north, the Qiangtang-Songpan terrane in the south, and the West Kunlun orogenic belt  
112 separated by the Altyn Tagh strike-slip fault in the northwest (Li et al., 2018a; Meng et al., 2017;  
113 Song et al., 2018b; Wang et al., 2022b; Zhang et al., 2012; Zhang et al., 2015b) (Figs. 1A and 1B).  
114 The EKOB is subdivided into three tectonic belts. These include the North and South Kunlun belts,  
115 and the Muz Tagh-Anemaqen and Hoh Xil-Bayan Har Terranes by the North Kunlun Fault (NKLF),  
116 Middle Kunlun Fault (MKLF), South Kunlun Fault (SKLF), Muz Tagh-Anemaqen Fault (MAF),  
117 from north to south (Jiang et al., 1992; Luo et al., 1999; Meng et al., 2013b; Yang et al., 1986; Yu et  
118 al., 2020b).

119 The North Kunlun belt is composed of Precambrian metamorphic rocks, late Paleozoic  
120 volcanic-sedimentary rocks, and Paleozoic and Triassic granitoids. The Precambrian rocks are  
121 dominated by gneisses, migmatite and amphibolite of the Paleoproterozoic Jinshuikou Group (Jiang  
122 et al., 1992) and the greenschist facies carbonate and clastic rocks of the Mesoproterozoic Binggou  
123 Group (Meng et al., 2018). Zircon U–Pb ages of the gneiss and amphibolite from the Jinshuikou



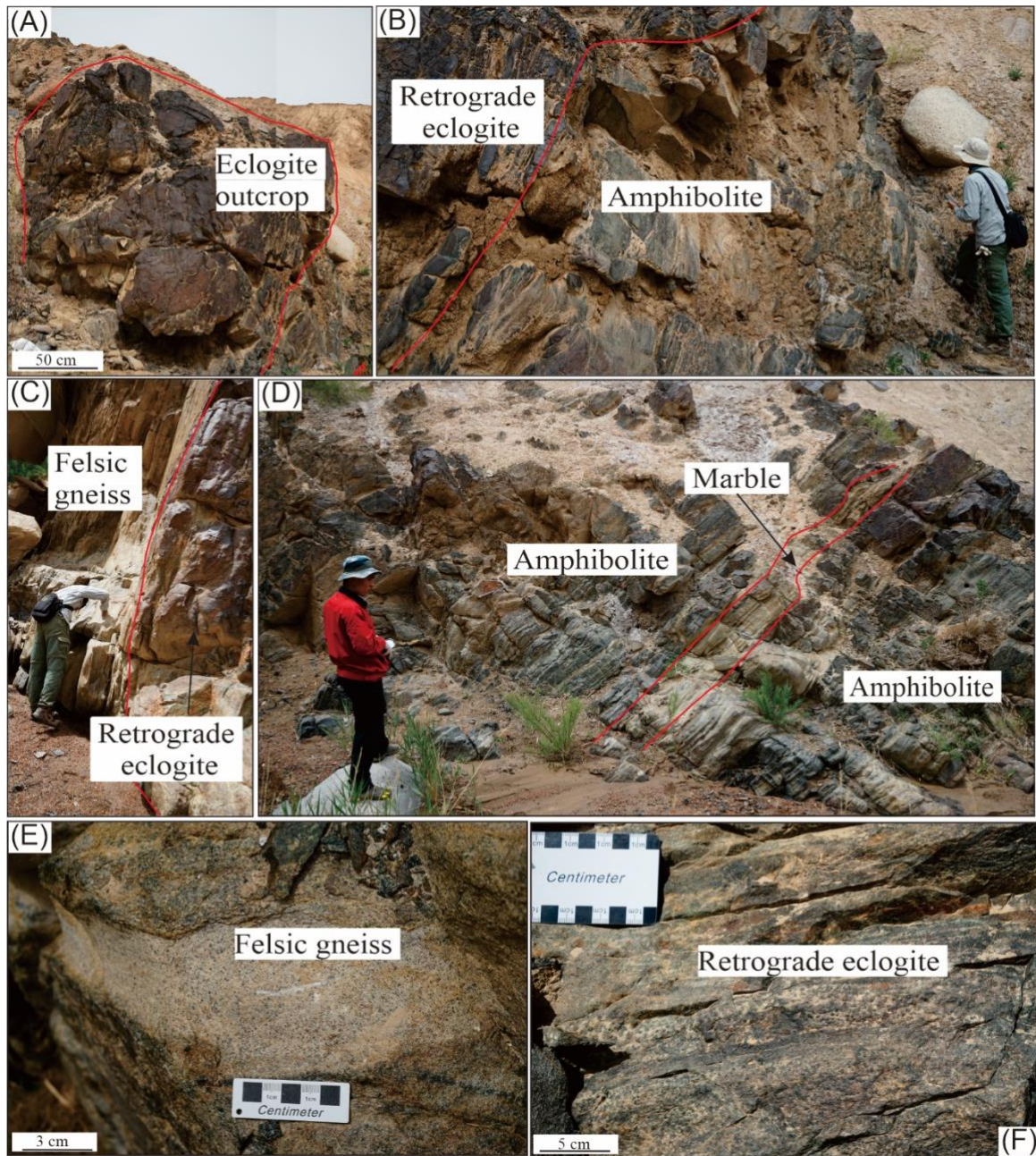
124 Group suggest that high-grade metamorphism at ca. 1.8 Ga was followed by a two-phase tecto-  
125 thermal event at ca. 1.0–0.9 Ga and ca. 400 Ma (Chen et al., 2008a; He et al., 2016; Meng et al.,  
126 2013a; Song et al., 2018b; Zhou et al., 2020). Zircon ages of the schists from the Xiaomiao Group  
127 point to the deposition of metasedimentary rocks during the Mesoproterozoic and subsequent  
128 metamorphism at ca. 400 Ma (He et al., 2016; Wang et al., 2003a). These basement rocks were later  
129 overlain by late Paleozoic volcanic-sedimentary rocks. Three phases of magmatism events, which  
130 include the Neoproterozoic gneissic granites deposited at ca. 1006–870 Ma (Chen et al., 2015;  
131 Meng et al., 2013b). The ca. 466–390 Ma Paleozoic diorites and granites and the ca. 250–200 Ma  
132 Triassic granites, formed in this belt (Dong et al., 2018).

133 The South Kunlun belt (SKT) is mainly composed of Paleozoic–Triassic sedimentary and  
134 volcanic rocks, with some Precambrian facies and Early Paleozoic and Permian–Triassic granites. It  
135 stretches from the Wenquan area in the east, through the Wanbaogou area in the middle, to Chader  
136 Tagh in the west. This succession witnessed the Caledonian to Indosinian events, including the  
137 Wanbaogou island arc and the Qingshuiquan back arc basin activities. Although the Qingshuiquan  
138 ophiolites and the volcanic rocks of the Wanbaogou Formation are the key indicators, their  
139 formation age and genetic settings have been disputed (Chen et al., 2011; He et al., 2016; Liu et al.,  
140 2016; Xu et al., 2016; Yu et al., 2020b).

141 The Central East Kunlun arc-accretionary complex belt is represented by the 540–460 Ma Early  
142 Paleozoic ophiolite, the 550–390 Ma arc volcanic and sedimentary rocks, widely regarded as a  
143 subduction-collision suture zone (Dong et al., 2018; Li et al., 2018b; Meng et al., 2015b; Yang et al.,  
144 2004; Zhou et al., 2020). Eclogite facies rocks are sporadically distributed in the Xiarihamu in the  
145 west, and Kehete and Wenquan areas in the east, forming a >500 km HP–UHP metamorphic belt

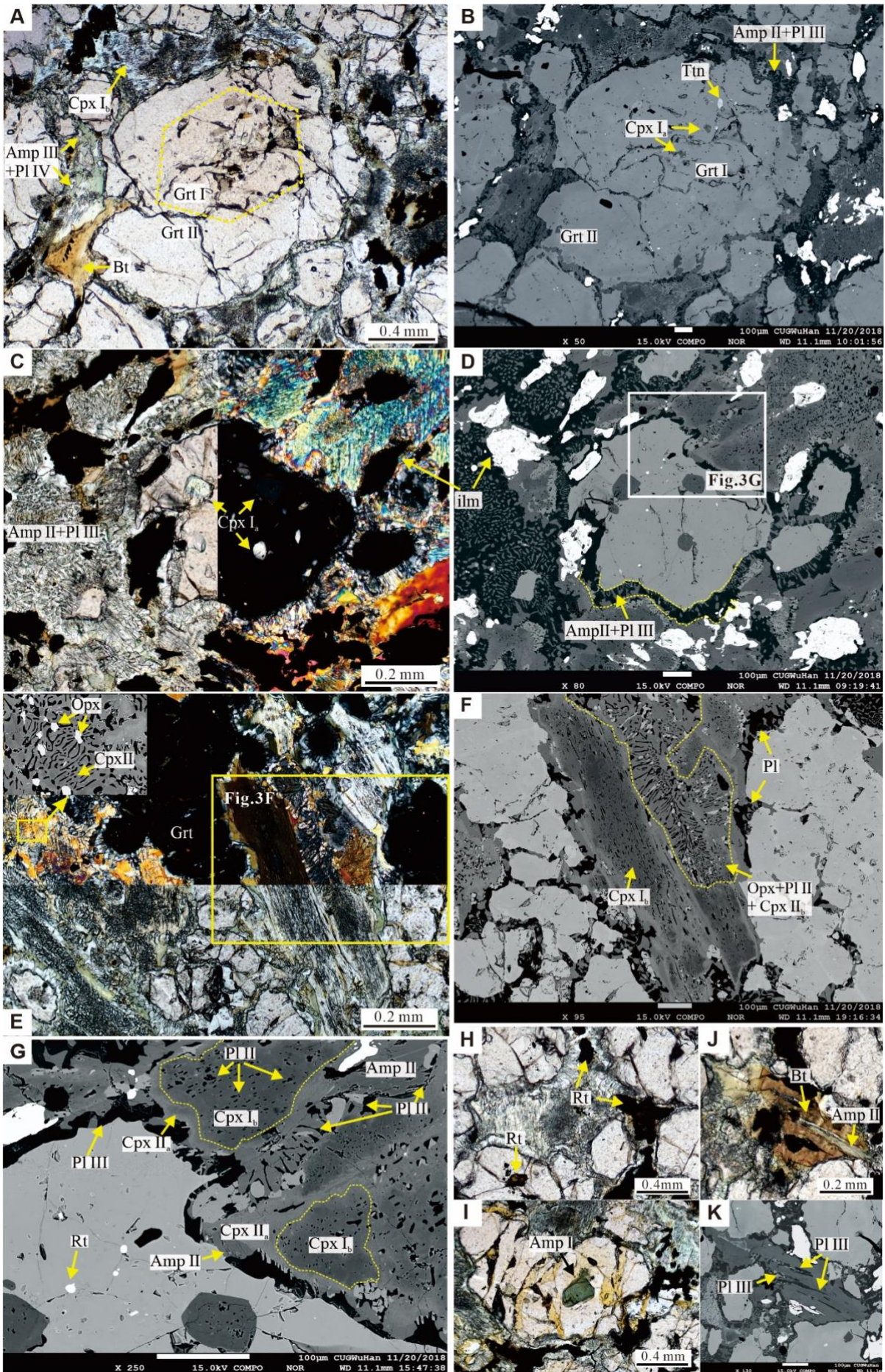
146 (Meng et al., 2013b; Qi et al., 2014; Qi et al., 2016b). Recently, coesite-bearing UHP metamorphic  
147 rocks were discovered in the Kehete area in the eastern segment (Fig. 1B)(Bi et al., 2018; Bi et al.,  
148 2020).

149 Eclogites were newly found at the Nuomuhong valley approximately 150 km SE from Golmud  
150 city in the central segment of the HP–UHP metamorphic belt in East Kunlun (Fig. 1B). Lithologies  
151 at Nuomuhong are comprised mainly of granitic gneiss, eclogite, and amphibolite with minor  
152 marble composition (Figs. 1C and 2). Eclogite occurs as lenses or blocks of 5–15 meters in diameter  
153 enclosed in the host gneiss of the Paleoproterozoic Jinshuikou Group (Figs. 1C and 2A, C). The  
154 eclogite has mainly been retrogressed (Fig. 2B, F) and at places, amphibolite can be found at the  
155 outer edge of the eclogite block (Fig. 2B). The Amphibolite occurs as massive or foliated structures,  
156 with some intercalated marble lenses/slices (Fig. 2D). In a ~500-meter-long cross-section from east  
157 to west along the Nuomuhong valley, dozens of eclogite and/or retrograde eclogite were sampled  
158 from three eclogite blocks (Figs. 1C and 2D). Three samples (LH3–2, LH3–4 and LH3–5) were  
159 selected for detailed petrographic observations and mineral chemistry analyses. In addition, the  
160 eclogite sample LH3–4 was performed for phase equilibrium modeling and SHRIMP U–Pb dating.  
161 The host felsic gneiss shows a granoblastic texture and consists of mainly plagioclase, potassium  
162 feldspar, quartz and biotite, with minor garnet (Fig. 2C–E). Twelve samples including 10 retrograde  
163 eclogites and 2 garnet amphibolites were selected for whole-rock major and trace element analyses.  
164 Mineral abbreviations are after Whitney and Evans (2010).



165

166 **Figure 2.** Field photographs of eclogite at Nuomuhong, in East Kunlun. (A) Eclogite block enclosed in the  
 167 host felsic gneiss. (B) Eclogite retrograded to amphibolite at edges. The red dashed line marks the boundary  
 168 between the retrograde eclogite and amphibolite. (C) The red dashed line showing the boundary between  
 169 retrograde eclogite and the host felsic gneiss. (D) Marble intercalated in amphibolite that shows a foliated  
 170 structure. (E) The host felsic gneiss consisted mainly of felsic minerals, biotite and garnet. (F) The retrograde  
 171 eclogite consisted of mainly garnet, clinopyroxene, amphibole and quartz.



173 **Figure 3.** Photomicrographs of representative eclogites at Nuomuhong, EKOB. (A) A large garnet  
174 porphyroblast from the eclogite LH3–5 showing apparent zoning with abundant inclusions in the reddish  
175 core and minor in the light rim. Amphibole (Amp II), plagioclase, ilmenite and biotite (Bt) developed around  
176 the garnet. (B) Backscattered electron image (BSE) of the garnet porphyroblast in panel A showing  
177 inclusions of titanite (Ttn) and omphacite (Cpx I<sub>a</sub>) in the core. (C–D) Corona of plagioclase (Pl III) +  
178 amphibole (Amp II) ± ilmenite (LH3–4) around a relict garnet porphyroblast with inclusions of omphacite  
179 (Cpx I<sub>a</sub>). Symplectite of plagioclase (III) + amphibole develops in the matrix; (E–F) Symplectite of  
180 orthopyroxene (Opx)+ plagioclase (Pl II) around relict omphacite in matrix from the sample LH3–4. Corona  
181 of symplectite amp II + Pl develops around relict garnet and low-sodic clinopyroxene (Cpx II<sub>a</sub>; light-colored  
182 in BSE) develops around relict omphacite porphyroblast (Cpx I<sub>b</sub>; dark-colored in BSE). (G) Locally enlarged  
183 BSE image in panel D showing transition from relict omphacite porphyroblast (Cpx I<sub>b</sub>; with no Opx) to  
184 clinopyroxene porphyroblast (Cpx II<sub>b</sub>; with Opx), then to symplectite of Amp II + Pl II; (with Opx). Corona  
185 of plagioclase (Pl III) + amphibole (Amp II) rims garnet; (H) Rutile inclusions in garnet or in matrix from the  
186 sample LH3–2, showing partial replaced by ilmenite; (I) Amphibole (Amp I) included in garnet from sample  
187 LH3–2. (G–K) Plane-polarized photo with corresponding BSE image showing Biotite around amphibole  
188 (Amp II) from sample LH3–5.

189

## 190 **PETROLOGY**

### 191 **Petrography and Mineral Compositions**

192 Representative minerals were analyzed using a JEOL JXA–8230 electron probe micro-analyzer  
193 (EPMA) in China University of Geosciences (Wuhan). The detailed analytical method and results  
194 listed in Supplementary Text and [Table S1-S6](#), respectively. The Nuomuhong EKOB eclogites are

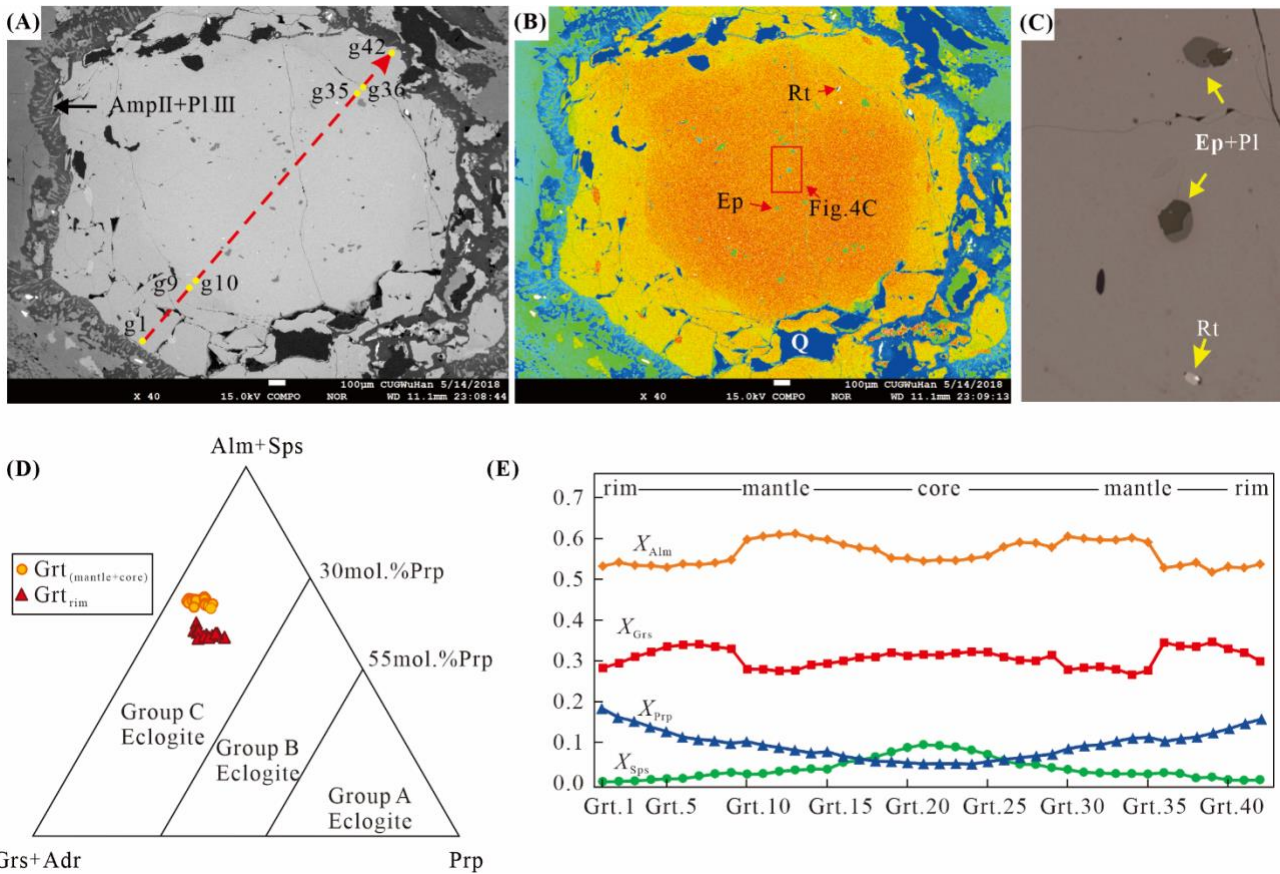
195 generally characterized by a massive structure with porphyroblastic/granoblastic texture. They  
196 comprise mainly 30–40 vol.% garnet, 25–30 % clinopyroxene, 15–20 % amphibole, 10–15 %  
197 plagioclase and 2–5 % biotite, with minor 2–5 % orthopyroxene and 1–3 % quartz, and accessory  
198 rutile/ilmenite, apatite, titanite and zircon (Fig. 3).

199

## 200 ***Garnet***

201 Euhedral to subhedral 0.2–2.0 mm grain size crystals typically characterize the porphyroblastic  
202 garnet minerals in representative sample LH3-2, LH3-4 and LH3-5. The garnet crystals typically  
203 contain a greater amount of omphacite, rutile/ilmenite/titanite, epidote + plagioclase, amphibole  
204 and quartz inclusions in the reddish core, compared to the light-colored rim (Fig. 3A, B; Fig. 4C).  
205 These observations are consistent with an apparent core-rim structure revealed by back-scattered  
206 electronic (BSE) photos (Fig. 3A, B; Fig. 4B). The garnet minerals commonly show an embayed  
207 texture and tend to be replaced by amphibole, plagioclase and an ilmenite corona (Fig. 3A-D, G). In  
208 places, aggregated epidote minerals and albite develop as inclusions in the garnet (Fig. 4C).

209 A chemical profile for one large garnet porphyroblast in the eclogite sample LH3-4 shows  
210 clear compositional zonation for almandine, pyrope, grossular and spessartine (Fig. 4D, E). From  
211 core to rim,  $X_{\text{Alm}} [= \text{Fe}^{2+}/(\text{Fe}^{2+} + \text{Mg} + \text{Ca} + \text{Mn})]$  increases from 0.55 to 0.61, and then decreases to  
212 0.52;  $X_{\text{Grs}} [= \text{Ca}/(\text{Fe}^{2+} + \text{Mg} + \text{Ca} + \text{Mn})]$  decreases slightly from 0.32 to 0.28, before a sharp  
213 increase to 0.34 and then decreases again to 0.28;  $X_{\text{Prp}} [= \text{Mg}/(\text{Fe}^{2+} + \text{Mg} + \text{Ca} + \text{Mn})]$  increases  
214 from 0.05 to 0.18; and  $X_{\text{Sps}} [= \text{Mn}/(\text{Fe}^{2+} + \text{Mg} + \text{Ca} + \text{Mn})]$  decreases from 0.09 to <0.01. The  $X_{\text{Sps}}$   
215 profile shows a classic bell-shaped zoning pattern, interpreted to represent growth zonation.



216  
 217 **Figure 4.** (A–B) BSE photographs of a large porphyroblastic garnet (LH3-4). The red dashed line represents  
 218 cross section analysis by EPMA. (C) Enlarged photo in panel B with aggregated inclusions of Ep + Pl. (D)  
 219 Diagram showing compositional variations of garnet. Both Grt<sub>(mantle+core)</sub> (Grt I) and Grt<sub>rim</sub> (Grt II) are  
 220 suggested to belong to group C-type according to Coleman et al. (1965). (E) Zoning profile of  $X_{Alm}$ ,  $X_{Sps}$ ,  $X_{Prp}$   
 221 and  $X_{Grs}$  across garnet in the eclogite samples LH3-4 from Nuomuhong.

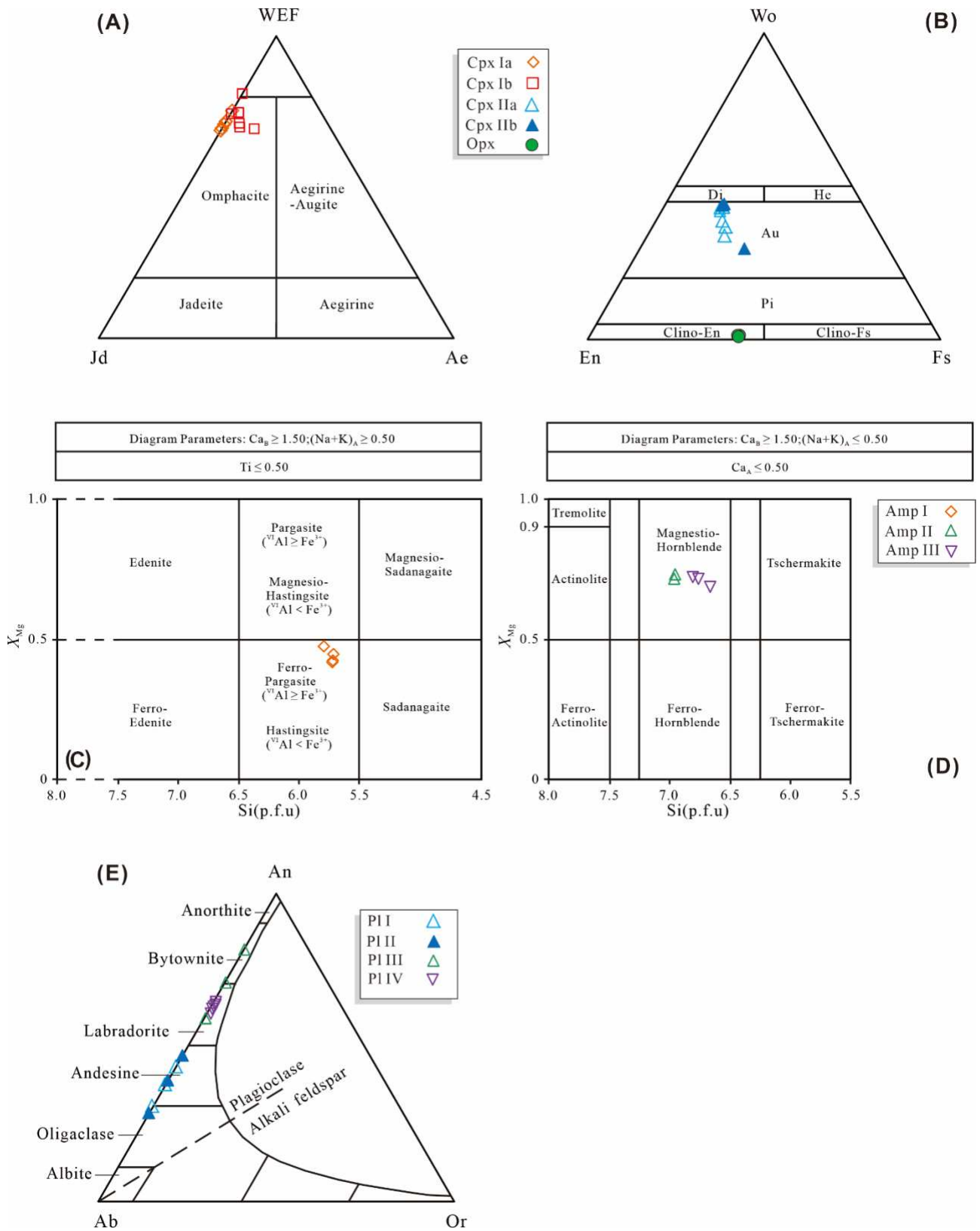
222

### 223 *Clinopyroxene*

224 Based on variations of occurrences and mineral compositions, clinopyroxene in sample LH3–4  
 225 show the following 4 archetypal subdivisions: (1) Cpx I, omphacite present as Cpx I<sub>a</sub>, inclusions in  
 226 garnet (Figs. 3C–D) or as Cpx I<sub>b</sub> matrix rock-forming minerals (Figs. 3A and 3C–3E). Most of Cpx  
 227 I<sub>b</sub> phases are partially replaced by low-sodium clinopyroxene and plagioclase-containing  
 228 symplectite. Cpx I<sub>a</sub> generally has higher Jd content than Cpx I<sub>b</sub> (Fig. 5A); (2) Cpx II occurs as Cpx

229 II<sub>a</sub> together with plagioclase-constituting symplectite Cpx I<sub>b</sub> rims, or as Cpx II<sub>b</sub> together with  
230 orthopyroxene and plagioclase replacing Cpx II<sub>a</sub>. The Cpx II<sub>a</sub> phases generally possess a higher Jd  
231 composition with lower MgO and FeO contents than Cpx II<sub>b</sub> (Table S2-S3, Fig. 5B). Both Cpx II<sub>a</sub>  
232 and Cpx II<sub>b</sub> have lower SiO<sub>2</sub> and Jd component, but higher MgO and FeO concentration than Cpx I  
233 (Table S2-S3, Fig. 5B). Away from Cpx I, Cpx II presents a lighter color in BSE images (Figs. 3E  
234 and 3F), showing increasing Wo enrichment (Fig. 5B).





235  
 236 **Figure 5.** Mineral chemistry diagrams. (A–B) Ternary classification diagrams for clinopyroxene from the  
 237 Nuomuhong eclogites, after [Morimoto \(1988\)](#); (A) Classification diagram for Quad–Jd–Ae; (B)  
 238 Classification diagram for Wo–En–Fs. (C–D) Classification diagrams for amphiboles for the Nuomuhong

239 eclogite, after [Leake et al. \(2004\)](#) and [Song et al. \(2018b\)](#). (E) Ab–An–Or diagram showing the  
 240 composition of plagioclase, after [Smith \(1974\)](#);  $Ab=X_{Na}=Na/(Ca + K + Na)$ ;  $An=X_{Ca}=Ca/(Ca + K + Na)$ ; Or  
 241  $=X_K=K/(Ca + K + Na)$ .

Stage Mineral	M <sub>1</sub>	M <sub>2</sub>	M <sub>3</sub>	M <sub>4</sub>	M <sub>5</sub>
Grt	—————				
Omp					
Cpx	—————				
Opx	—————				
Amp	—————				—————
Bt					—————
Pl			—————		
Rt	—————				
ilm			—————		
Phn		-----			

242

243 **Figure 6.** Sequences of mineral assemblages for different metamorphic stages. Solid lines indicate minerals  
 244 present in the samples, whereas the dashed line refers to inferred minerals.

245

### 246 *Amphibole*

247 Amphibole in sample LH3–4 occurs as inclusions ([Fig. 3I](#)) in garnet (Amp I), or together with  
 248 plagioclase as corona ([Fig. 3C–3E](#)) around garnet (Amp II), or as rock-forming minerals in matrix  
 249 (Amp III, [Figs. 3A and 3B](#)). Amp I exhibits a lower Si content of 5.71–5.72 (p.f.u.) with a higher  
 250 <sup>IV</sup>Al composition of 2.22–2.29 (p.f.u.). Its Mg<sup>#</sup> [= (Mg/(Mg+Fe<sup>2+</sup>))] of 0.42–0.45 and (Na+K)<sub>A</sub> ≤  
 251 0.50 (p.f.u.), corresponds to ferro-pargasite ([Fig. 5C](#)) according to [Leake et al. \(1997\)](#). Compared to  
 252 Amp I, a higher Si content of 6.95–6.96 (p.f.u.) and lower <sup>IV</sup>Al content of 1.04–1.05 (p.f.u.),  
 253 characterizes Amp II. Both Amp II and Amp III have similar Mg<sup>#</sup> of 0.69–0.72 and (Na+K)<sub>A</sub> ≤ 0.50  
 254 (p.f.u.), indicative of a magnestio-hornblende composition ([Table S4, Fig. 5D](#)).

255

256 ***Plagioclase***

257 Plagioclase occurs either as inclusions in garnet (Fig. 4C), or together with matrix amphibole,  
258 clinopyroxene and/or orthopyroxene (Fig. 3D, G). When included in garnet, plagioclase (LH3-2, Pl  
259 I) co-exists with epidote, constituting composite inclusions and is albite (Fig. 4C). Matrix  
260 plagioclase (LH3-4, Pl II) either forms symplectite after omphacite (Fig. 3E, F, G), or occurs  
261 together with Amp II in the corona surrounding garnet (LH3-5, Pl III) (Fig. 3D, G). In places, large  
262 LH3-2 Pl IV plagioclase shows texture equilibration with Amp III amphibole (Fig. 3A). On the  
263 other hand, An<sub>28-47</sub>Ab<sub>53-72</sub> Pl II plagioclase has an oligoclase-andesine affinity, whereas the An<sub>61-</sub>  
264 <sub>64</sub>Ab<sub>36-39</sub> Pl III and An<sub>60-82</sub>Ab<sub>18-40</sub> Pl IV forms, characterized by higher An values, are related to  
265 labradorite (Fig. 5E, Table S5).

266  
267 ***Orthopyroxene***

268 Fine-grained matrix Opx (LH3-2) develops mainly in association with Pl II and Cpx II<sub>b</sub>-  
269 containing symplectite after Cpx II<sub>a</sub> (Fig. 3E-3G). In the Wo-En-Fs diagram, Opx is shown to  
270 belong to hypersthene with X<sub>En</sub> of 56.3-56.9 and X<sub>Fs</sub> of 41.8-42.4 (Table S6, Fig. 5B).

271  
272 ***Minor minerals***

273 The occurrence of minor fine-grained biotite in the matrix (LH3-4) and around garnet (Fig. 3A) or  
274 amphibole (Fig. 3J), is interpreted to represent the formation of phengite during early  
275 metamorphism (Fig. 6). Epidote and anorthosite exist as composite inclusions in garnet but absent  
276 in the matrix (Fig. 4C). Rutile, partially replaced by ilmenite/titanite, is present both as inclusions in  
277 garnet and in the matrix (Figs. 3H and 4C).

278

## 279 **Minerology and metamorphic stages**

280 Based on petrographic observations and mineral compositions, the following five mineral  
281 assemblages can be inferred for the eclogite at Nuomuhong, east Kunlun: (1) M<sub>1</sub> prograde  
282 metamorphic stage amphibole eclogite facies evidenced by Cpx I<sub>a</sub> + Amp I + Rt + Ep + Qz  
283 inclusions in garnet core and mantle/garnet core-mantle compositions; (2) Metamorphic M<sub>2</sub> peak  
284 stage eclogite facies evidenced by Grt rim, matrix rock-forming Cpx I<sub>b</sub>, Rt and quartz. Omphacite  
285 inclusions in zircons from Group #2 (Fig. 7) are further inferred to belong to metamorphic peak  
286 stage mineral assemblage; (3) Early retrograde metamorphic stage high-pressure granulite facies  
287 (M<sub>3</sub>), is substantiated by Cpx II<sub>a</sub> with low Jd symplectite content and plagioclase (Pl II) rimming  
288 Cpx I<sub>b</sub>; (4) Subsequent retrograde metamorphic stage medium-pressure granulite facies (M<sub>4</sub>)  
289 represented by garnet surrounding Opx coronas and Opx + Pl II + Cpx II<sub>b</sub> replacing Cpx II<sub>a</sub>  
290 symplectite; (5) Later retrograde metamorphic stage amphibolite facies (M<sub>5</sub>) indicated by Amp II  
291 and Pl II garnet-surrounding intergrowth and large-grained matrix Pl IV and Amp III. In addition,  
292 Ilm replacing Rt and the occurrence of matrix Bt (replacing phengite), likely formed at this stage  
293 (Fig. 6).

294

## 295 **METAMORPHIC *P-T* CONDITIONS**

296 In this study, to reconstruct the metamorphic *P-T* path for eclogite formation at Nuomuhong,  
297 we selected representative eclogite LH3–4 samples for further study based on the progressive  
298 growth zonation retained in porphyroblastic garnet and the relatively complete mineral sequences  
299 recorded in these samples. We use both conventional geothermobarometry and phase equilibrium

300 modelling to constrain  $P$ – $T$  conditions for different metamorphic stages.

301

### 302 **Conventional Geothermobarometry**

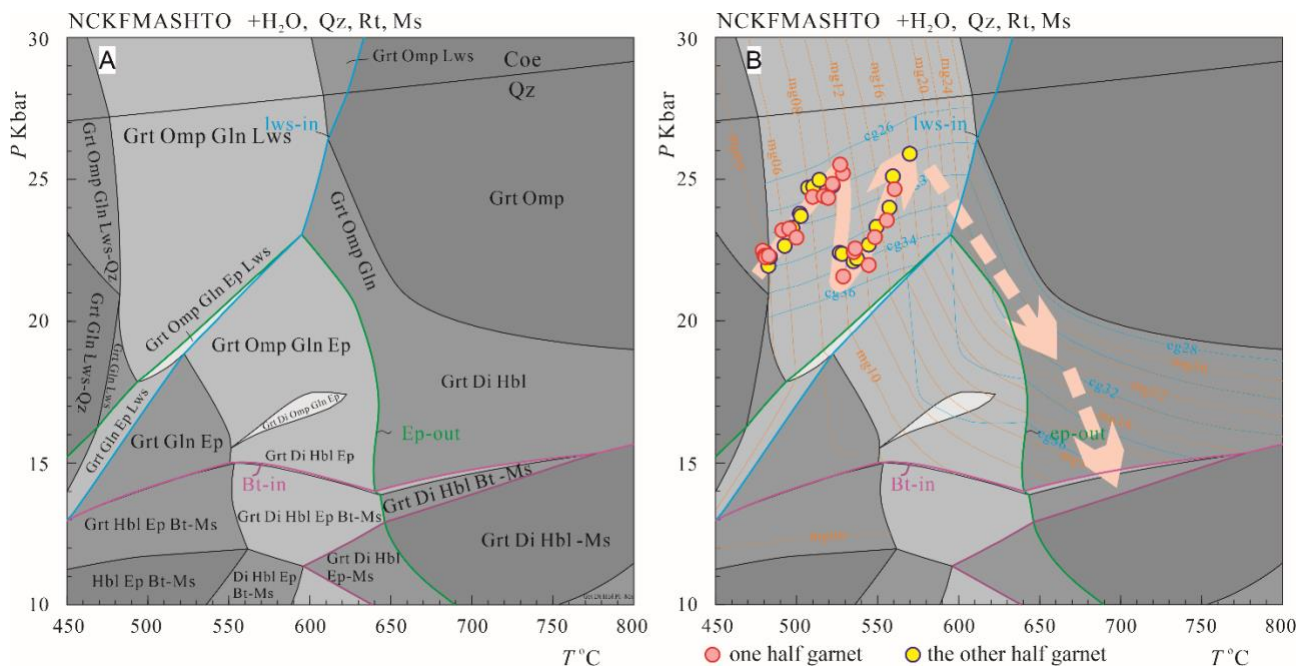
303 Conventional geothermobarometry, including the garnet–clinopyroxene (Grt–Cpx)  
304 thermometry (Ravna, 2000), the Al-in-hornblende barometry (Schmidt, 1992) combined with the  
305 amphibole–plagioclase (Amp–Pl) thermometry (Holland and Blundy, 1994), and the two-pyroxene  
306 thermometry (Wood, 1973) were used for  $P$ – $T$  estimates for different stage mineral assemblages.  $P$ –  
307  $T$  conditions for prograde stage ( $M_1$ ) metamorphism calculated using the Grt–Cpx thermometry on  
308 garnet-core (Grt I) composition, and omphacite (Cpx I<sub>a</sub>), indicate formation at metamorphic  
309 pressure >14 kbar and temperature of 470–506 °C. Grt–Cpx thermometry on garnet rim (Grt II) and  
310 matrix omphacite (Cpx I<sub>b</sub>), suggest peak stage metamorphism ( $M_2$ ) occurred at a temperature range  
311 of 525–585 °C at a pressure of 20 kbar according to previous studies on eclogite from the EKOB  
312 (Meng et al., 2015b; Qi et al., 2014; Qi et al., 2016b; Song et al., 2018b). Calculated retrograde  
313 stage ( $M_4$ ) metamorphic temperature of 860–900 °C using the two-pyroxene thermometry and  
314 compositions of orthopyroxene (Opx) and low-sodic clinopyroxene (Cpx II<sub>b</sub>), assumes a medium  
315 pressure of 6 kbar. The  $P$ – $T$  conditions for late retrograde stage metamorphosis ( $M_5$ ) using Al-in-  
316 hornblende barometry, Amp–Pl thermometry and compositions of large matrix amphibole (Amp III)  
317 and plagioclase (Pl IV), point to formation at ~6 kbar and 710–730 °C (Fig. 6).

318

### 319 **Phase Equilibrium Modelling**

320 Phase diagrams were drawn using the updated March 2014 THERMOCALC software version  
321 3.40, and the November 2016 updated version of the associated internally consistent

322 thermodynamic dataset ds62 (Holland and Powell, 2011). The NCKFMASHTO system Na<sub>2</sub>O–  
 323 CaO–K<sub>2</sub>O–FeO–MgO–Al<sub>2</sub>O<sub>3</sub>–SiO<sub>2</sub>–H<sub>2</sub>O–TiO<sub>2</sub>–O chemical composition was selected for analysis,  
 324 with *a*–*x* relationships implemented as follows: amphibole and clinopyroxene (Green et al., 2016);  
 325 garnet, phengitic muscovite and biotite (White et al., 2014); epidote (Holland and Powell, 2011).  
 326 Rutile, lawsonite, quartz and H<sub>2</sub>O were considered to be in the pure phase. Bulk rock XRF  
 327 composition was used for modelling after correction of CaO, SiO<sub>2</sub>, Al<sub>2</sub>O<sub>3</sub> contents for the P<sub>2</sub>O<sub>3</sub> and  
 328 MnO contained in apatite and spessartine. Fe<sub>2</sub>O<sub>3</sub> was determined by wet chemistry. The corrected  
 329 bulk composition in mol% used in phase equilibrium modeling was SiO<sub>2</sub> (51.99), Al<sub>2</sub>O<sub>3</sub> (8.51),  
 330 CaO (11.82), MgO (11.21), FeO (12.26), K<sub>2</sub>O (0.11), Na<sub>2</sub>O (2.17), TiO<sub>2</sub> (0.92) and O (1.0). H<sub>2</sub>O  
 331 was assumed to be in excess, considering the abundance of various hydrous mineral inclusions (e.g.,  
 332 epidote and amphibole) in garnet.



333  
 334 **Figure 7.** (A) *P*–*T* pseudosection for eclogite LH3–4 at Nuomuhong in the NCKFMASHTO system. Mineral  
 335 abbreviations follow Thermocalc dataset (B). cg and mg represent calculated isopleths for grossular  
 336 [Ca/(Ca+Mg+Fe+Mn)] and pyrope [Mg/(Ca+Mg+Fe+Mn)] endmembers in garnet, respectively. For instance,

337 mg06 denotes 0.06 pyrope and cg26 0.26 grossular. Mineral abbreviations are after [Whitney and Evans](#)  
338 [\(2010\)](#).

339 The  $P$ - $T$  pseudosection for the retrograde eclogite LH3-4 had a  $P$ - $T$  range of 10–30 kbar and  
340 450–800 °C ([Fig. 7](#)). Figure 8A places the phase assemblage fields of lawsonite at 12–30 kbar and  
341 400–600 °C and epidote at 10–23 kbar and 400–635 °C. Lawsonite is replaced by epidote at  $P$  <23  
342 kbar and  $T$  of <595 °C, and by garnet and omphacite at  $T$  >595 °C and  $P$  >17.5 kbar. In the phase  
343 assemblage fields of **Grt + Omp (Di) + Gln (Hbl) ± Ep + Qtz + Rt + Ms + H<sub>2</sub>O**, glaucophane  
344 gradually changes to hornblende and omphacite to diopside at decreasing pressure. The replacement  
345 of muscovite by biotite in the phase assemblage fields occurs at a  $P$  range of 14–15.5 kbar before  
346 being replaced again by hornblende and clinopyroxene at  $T$  >595 °C. Isopleths for 26–36 mol% Grs  
347 and 5–26 mol% Prp in garnet have been calculated for the  $P$ - $T$  range related to the Gln (Hbl)-  
348 bearing and Ms-bearing phase assemblage fields ([Fig. 7B](#)). In the law-bearing phase assemblage  
349 fields, isopleths for Grs in garnet have gentle to moderate positive slopes with Grs values  
350 decreasing with pressure, whereas isopleths of Prp in garnet have almost vertical slopes with Prp  
351 values increasing with temperature. In the law-absent phase assemblage fields, isopleths for Grs in  
352 garnet have vertical to moderate negative slopes with Grs values tending to decrease with rising  
353 temperature, whereas the garnet Prp isopleths have moderate negative slopes with Prp values  
354 increasing simultaneously with temperature.

355 The observed M<sub>2</sub> peak stage mineral assemblage corresponds to the modelled field with the  
356 phase assemblage of **Grt + Omp (Di) + Gln (Hbl) + Qtz + Rt + Ms + H<sub>2</sub>O** at 14.0–26.5 kbar and  
357 595–800 °C. However, isopleths for the measured Grs and Prp content in garnet (27–35 mol% and  
358 5–18 mol%, respectively) yield  $P$ - $T$  conditions of 21.5–26 kbar and 480–570 °C in the phase

359 assemblage field of Grt + Omp + Gln + Lws + Qtz + Rt + Ms + H<sub>2</sub>O (Fig. 7B). Both muscovite and  
360 lawsonite were not detected in the thin section. The modelled muscovite content in this phase  
361 assemblage field was <1.5 mode%. Its low contents may be the reason for non-detection by thin  
362 section analysis; or may be pointing to complete retrograde transformation to biotite during the late  
363 stage metamorphism as evidenced by the presence of matrix biotite (Fig. 3A, J). Lawsonite may  
364 have been present in the peak mineral assemblage but was subsequently replaced by amphibole and  
365 clinopyroxene with increasing exhumation  $T$  and or was replaced by epidote due to effective bulk  
366 rock composition in confined equilibration volume (Wei et al., 2010). Aggregates of Ep + Ab  
367 (potentially originating from paragonite) as inclusions in garnet may be pseudomorphs produced  
368 after lawsonite (Fig. 4C). Both situations correlate with dehydration reactions and may be easily  
369 triggered when  $T$  increases or  $P$  decreases. The inferred presence of lawsonite during prograde  
370 metamorphism has previously been reported in many HP/UHP eclogite terrane based on composite  
371 inclusions of Ep/Zo  $\pm$  Pg/Ab in garnet (Wei et al., 2010; Hamelin et al., 2018). For instance, in  
372 western Dabie, epidote inclusions, coupled with paragonite, was interpreted to reflect the former  
373 presence of lawsonite (Wei et al., 2010). In this study, because of intense retrogression during post-  
374 eclogite facies stages, the eclogite at Nuomuhong has been strongly retrograded with most garnet  
375 porphyroblast replaced by later stage mineral aggregates (e.g., amphibole, plagioclase and ilmenite).  
376 However, the well-preserved garnet growth zoning for a carefully selected garnet porphyroblast  
377 indicates the prograde information could have been potentially preserved in this refractory mineral.  
378 Using phase equilibrium modeling and compositional isopleth geothermobarometry, we interpret  
379 the  $P$ – $T$  regime of 21.5–26 kbar and 480–570 °C for lawsonite stability to represent possible  
380 prograde stage  $P$ – $T$  conditions.



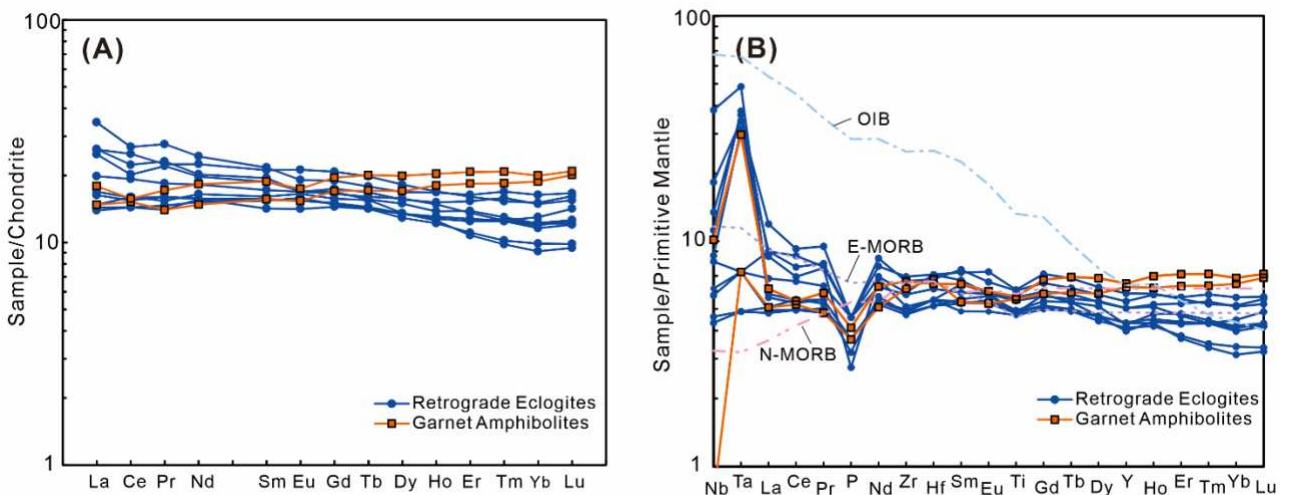
381 Therefore, the inferred peak mineral assemblage of Grt + Omp + Amp + Qz + Rt at the M<sub>2</sub>  
382 stage to correspond to the modelled phase assemblage field of Grt + Omp + Gln + Lws + Qz + Rt +  
383 Ms + H<sub>2</sub>O at *P* of 21.5–26 kbar and *T* of 480–570 °C. Glaucofane may have been gradually  
384 replaced by Na-poor amphibole during decompression. Amphibole inclusion in garnet with higher  
385 Na content than that in the matrix, may be assumed as support for this conclusion. Besides,  
386 variations of endmembers across the garnet could be indicative of two-stage garnet porphyroblast  
387 growth with various *P–T* evolutions, first controlled by increasing pressure and temperature,  
388 followed by a second rise in pressure and temperature and then by an eventual decrease in pressure  
389 (Fig. 7B). During initial exhumation, lawsonite decomposed and the *P–T* path crossed the modelled  
390 phase assemblage of Grt + Omp (Di) + Gln (Hbl) + Qz + Rt + Ms + H<sub>2</sub>O with *P–T* conditions of  
391 14.0–26.5 kbar and 595–800 °C. Further exhumation led to the transition of muscovite to biotite  
392 and omphacite to diopside and plagioclase, which may correspond to the modelled phase  
393 assemblage field of Grt + Di + Hbl + Qz + Rt + Bt + H<sub>2</sub>O with *P–T* conditions of 13.0–15.5 kbar  
394 and 645–775 °C. However, with a change in the effective bulk rock composition due to the presence  
395 of garnet, this *P–T* regime remains uncertain. *P–T* conditions for the formation of orthopyroxene  
396 have not been constrained for the change of effective bulk rock composition.

397

## 398 **WHOLE-ROCK GEOCHEMISTRY**

399 The analytical procedure for whole rock geochemistry determination is listed in the  
400 Supplementary Text, and the results in Supplementary Table S7. The data show that the retrograde  
401 eclogites at Nuomuhong are basaltic in composition. They possess low SiO<sub>2</sub> (48.33–51.07 wt.%),  
402 high Al<sub>2</sub>O<sub>3</sub> (13.39–15.37 %) and CaO contents (10.39–12.75 %), and moderate TiO<sub>2</sub> (1.02–1.32 %)

403 and Cr (154–290 ppm) compositions. On the AFM [(Na<sub>2</sub>O+K<sub>2</sub>O) –FeO<sup>T</sup>–MgO] diagram, all data  
 404 fall in the tholeiite series field (Fig. 11E). The retrograded eclogites are relatively low in total rare  
 405 earth elements abundance ( $\sum\text{REEs}=36.31\text{--}59.19$  ppm). On the chondrite-normalized REE diagram  
 406 (Fig. 8A), they exhibit nearly flat to enriched REE patterns, without significant Eu anomalies  
 407 ( $\delta\text{Eu}=0.91\text{--}1.05$ ) and are slightly enriched LREE, with La<sub>N</sub>/Yb<sub>N</sub> ratios of 1.17–2.21. By contrast,  
 408 the garnet amphibolites exhibit slight LREEs depletion (La<sub>N</sub>/Sm<sub>N</sub>=0.79–0.90). Primitive mantle-  
 409 normalized trace element analysis (Fig. 8B), suggests the retrograde eclogites are strongly enriched  
 410 in Nb and Ta but depleted in Zr and Ti. On the other hand, the garnet amphibolites are enriched with  
 411 Zr, with Nb–Ta showing significant positive anomalies relative to La.

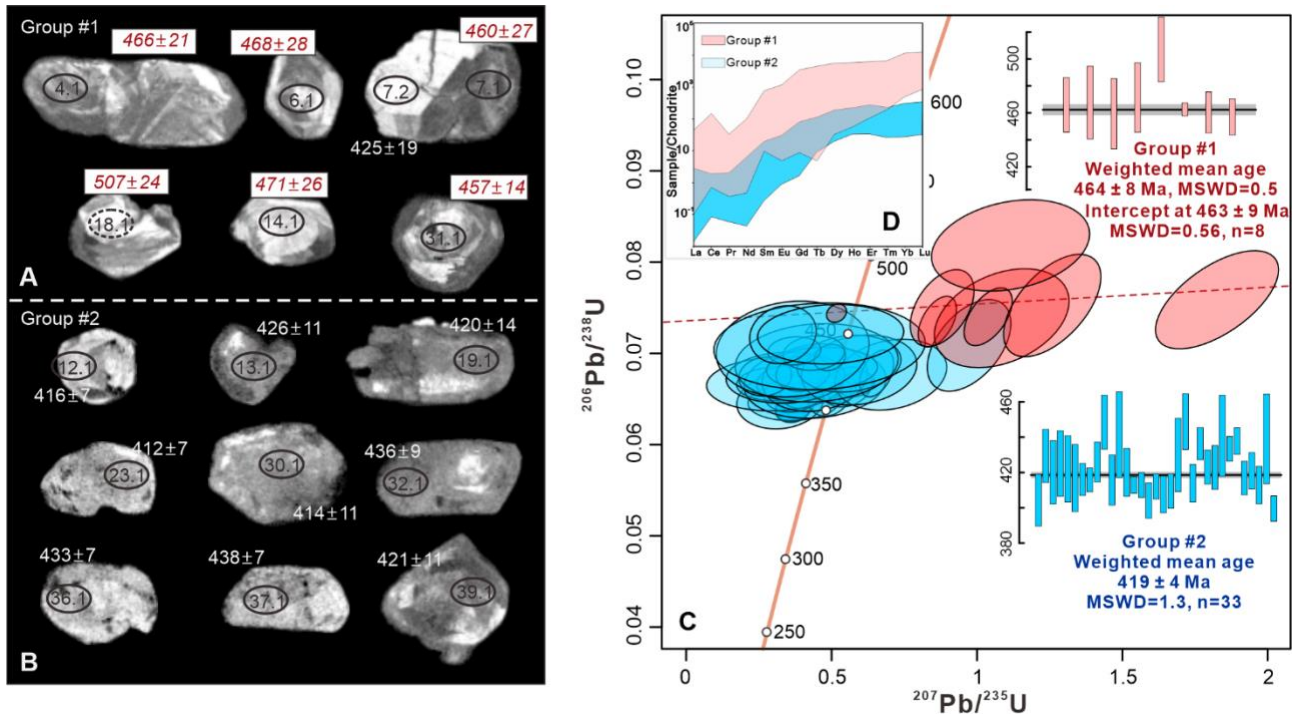


412  
 413 **Figure 8.** (A) Chondrite-normalized REE distribution patterns. (B) Plots for primitive mantle-normalized  
 414 retrograde eclogites and garnet amphibolites. The chondrite and primitive mantle values are from (Sun and  
 415 McDonough, 1989).

416  
 417 **ZIRCON U-Pb DATING**

418 Zircon grains from the LH3–4 eclogite display a euhedral to subhedral morphology, with a  
 419 tendency to be rounded, being 70–130  $\mu\text{m}$  in length. The majority of the zircons are homogeneous

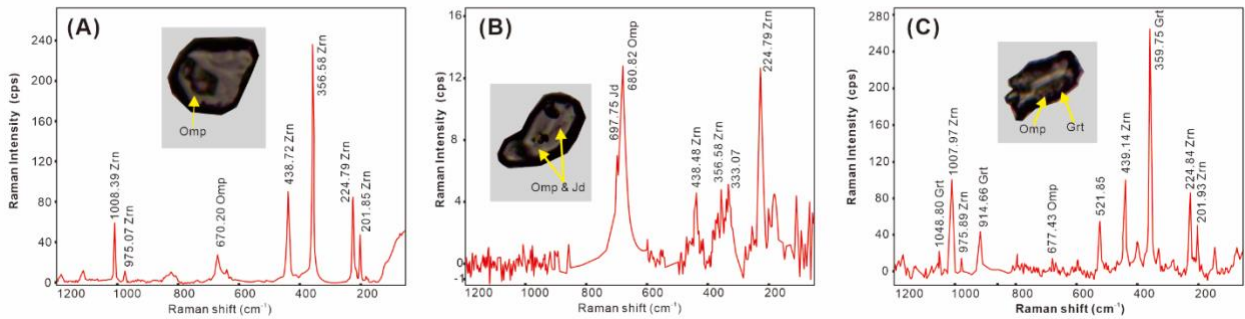
420 or show weak or sector zonation in cathodoluminescence (CL) images (Figs. 9A, B), a typical  
 421 characteristic of a metamorphic origin (Corfu et al., 2003; Wang et al., 2013b; Wu and Zhen, 2004).  
 422 Some grains have core-rim structures (Fig. 9A), broad zonation and contrast bright cores taken to  
 423 indicate residual cores that survived metamorphic alteration.



424  
 425 **Figure 9.** (A–B) Zircon CL images, (C) SHRIMP U–Pb age concordia diagram and weighted mean  
 426  $^{206}\text{Pb}/^{238}\text{U}$  ages, and (D) Chondrite-normalized REE distribution patterns for the Nuomuhong retrograde  
 427 eclogite LH3–4.

428 A total of 45 analyses were obtained by SHRIMP dating (Table S8). The Th and U contents of  
 429 most samples are low, with Th/U ratios <0.1. A majority of the analyses contain near flat heavy  
 430 REE (HREE) patterns in the chondrite normalized diagram (Fig. 9D). A few of the zircons reveal  
 431 Th/U ratios >0.1, interpreted as an attribute of the dissolution of Th-enriched minerals such as  
 432 epidote, under HT conditions (Hermann, 2002; Yu et al., 2013b). The weighted mean of  $^{206}\text{Pb}/^{238}\text{U}$   
 433 ages represented two groups, with Group #1 consisting of 8 analyses yielding an intercept age of

434 463±9 Ma with an MSWD of 0.56 and an identical weighted mean age of 464±8 Ma with an  
 435 MSWD of 0.5 (Fig. 9C). Group #2, comprised of 33 analyses, yielded a weighted mean age of  
 436 419±4 Ma with an MSWD of 1.3 (Fig. 9C). The laser Raman spectroscopy of the inclusions in the  
 437 second group zircons indicate a omphacite and garnet composition, suggesting that the Group #2  
 438 zircons represent a lower age limit for when peak eclogite facies metamorphism occurred (Figs.  
 439 10A–10C).



440  
 441 **Figure 10.** Raman spectra of (A) omphacite (Omp) inclusions, (B) omphacite/jadeite inclusions, and (C)  
 442 garnet (Grt) and omphacite inclusions in Group #2 zircon (Zrn) grains from the Nuomuhong retrograde  
 443 eclogite, middle East Kunlun orogen.

444  
 445 **DISCUSSION**

446 **Constraints on the Timing of Metamorphism**

447 Two distinct metamorphic age groups of 464±9 Ma (MSWD=0.5) and 419±4 Ma (MSWD=1.3)  
 448 were obtained from the Nuomuhong eclogites (Figs. 9) . The first-group zircons possess core–rim  
 449 structures with broad zoning and core contrast brightness suggestive of potential residual  
 450 metamorphic zircons. Though most of the zircons from these two groups yielded low Th/U ratios,  
 451 the first group shows a progressive increase in HREE patterns from Dy to Lu (Fig. 9D). We

452 interpret the first group of zircon age to approximate the age of eclogite protoliths, which is similar  
453 to the 520–460 Ma age inferred for regional ophiolite formation in this setting (Qi et al., 2016c) and  
454 the 471–454 Ma magmatic events of Proto-Tethys oceanic crust subduction (Fu et al., 2022b).

455 In contrast, the second-group zircons have typical morphological and textural characteristics of  
456 metamorphic zircons (Wu and Zheng, 2004), with similarly extremely low Th/U ratios (Table S8).  
457 During metamorphic recrystallization, Th is more likely to be expelled from the zircon lattice than  
458 U, accounting for the relatively low Th/U ratios observed. Laser Raman spectroscopy analyses of  
459 the inclusions in the second-group zircons reveals the presence of typical eclogite facies minerals  
460 like omphacite and garnet, indicating a younger age for the Group #2 zircons compared to peak-  
461 pressure metamorphism. The nearly flat HREE patterns further suggests these zircons grew in  
462 relatively high-pressure conditions in the presence of garnet (Fig. 9D). Therefore, we interpret the  
463 younger  $419\pm 4$  Ma age as the lower age limit for peak eclogite facies metamorphism. This age is  
464 consistent with previously reported (near) peak ages of 428–411 Ma for eclogites in other localities  
465 in the EKOB (Bi et al., 2020; Guo et al., 2020; Jia et al., 2014; Meng et al., 2013b; Pan and Zhang,  
466 2020; Qi et al., 2014; Qi et al., 2016b; Song et al., 2018b; Tang et al., 2022; Wang et al., 2012;  
467 Wang, 2020). In summary, our SHRIMP zircon U-Pb data suggest that the protoliths of the  
468 Nuomuhong eclogites could have been formed at  $\sim 464$  Ma, after which they experienced eclogite  
469 facies metamorphism prior to  $419\pm 4$  Ma, coincident with protolith and metamorphic ages from  
470 regional EKOB eclogites.

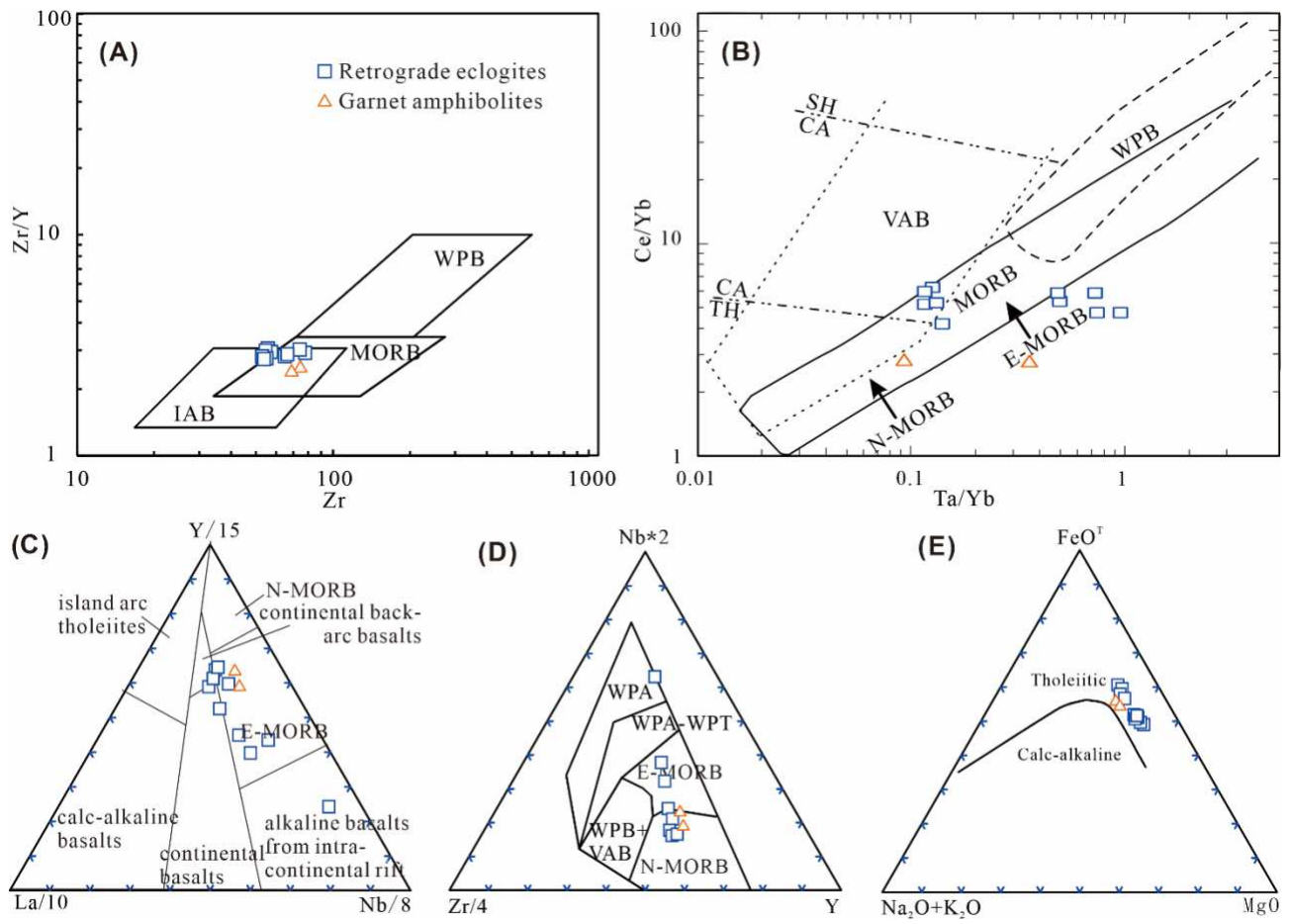
471

## 472 **Tectonic Affinity of Protoliths of the Eclogites**

473 Although eclogites may undergo complex prograde and retrograde metamorphic processes, the

474 study of eclogites in many orogenic belts indicate that the activity of external fluids did not cause  
475 obvious element migration, especially for the HFSE and REE (Wang et al., 2013a). In this study,  
476 the low loss on ignition of  $<0.38$  and the relatively coherent patterns in the normalized REE and  
477 trace element diagrams (Figs. 8A and 8B), suggest limited modification of most elements in the  
478 Nuomuhong eclogites. Here we use the fluid-immobile elements to fingerprint the tectonic  
479 protoliths of the Nuomuhong eclogites.

480 The Nuomuhong eclogites have low  $\text{SiO}_2$  in the range of 48.57–51.07 wt.%, and moderate  
481 1.04–1.32 wt.%  $\text{TiO}_2$ , 6.43–8.77 wt.%  $\text{MgO}$  and 154–290 ppm Cr contents, similar to tholeiitic  
482 basalts. In the normalized REE and trace element diagrams, most of the eclogite samples have near-  
483 flat and slightly enriched LREE, a characteristic reminiscent of N-MORB and E-MORB (Figs. 8A  
484 and 8B). The low Zr/Y ratios preclude an intra-plate origin, as supported by the Zr vs. Zr–Y cross  
485 plot (Fig. 11A). Tectonic discrimination utilizing exemplary HFSEs and REEs such as Nb, Ta, La,  
486 Ce, Yb and Y, allude to a majority of the samples converging on E-MORB and N-MORB within the  
487 MORB–OIB array (Figs. 11B–D), an indication of their derivation from MORB-type oceanic crust.  
488 These observations demonstrate that the protoliths of the Nuomuhong eclogites are essentially  
489 subducted MORB-like oceanic crust basalt or gabbro, similar to oceanic crust-derived eclogites in  
490 the eastern segment of the EKOB locality (Song et al., 2018b).

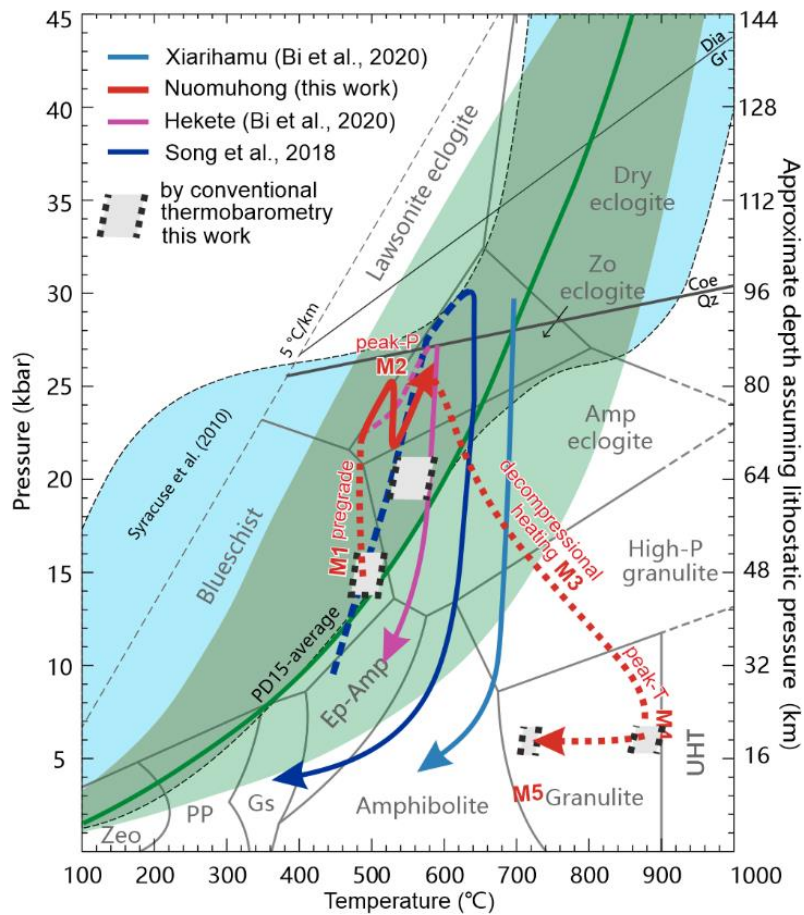


491  
 492 **Figure 11.** Tectonic discrimination diagrams (A–D) for the retrograde eclogite. (A) Zr–Zr/Y diagram  
 493 (Pearce and Norry, 1979); (B) Ce/Yb–Ta/Yb diagram (Pearce, 1982); (C) Y–La–Nb diagram (Cabanis and  
 494 Lecolle, 1989); (D) Nb–Zr–Y diagram (Meschede, 1986); (E) AFM diagram (Irvine and Baragar, 1971). W  
 495 corresponds to CA–calc-alkaline, MORB–mid-ocean ridge basalt, SH–shoshonitic, TH–tholeiitic, VAB–  
 496 volcanic arc basalt, WPB–within plate basalt.

498 **Metamorphic records for the oceanic subduction and continental collision in the northern**  
 499 **Proto-Tethys**

500 Based on petrographic observations, conventional geothermobarometry and phase equilibrium  
 501 modelling, five metamorphic stages and associated *P–T* conditions were determined for the  
 502 Nuomuhong eclogites, namely: (1) the prograde  $M_1$  stage with *P–T* conditions of >14.0 kbar/~470–

503 506°C; (2) the peak-*P* M<sub>2</sub> eclogite facies stage at ~26 kbar *P* and ~570°C *T*; (3) the early M<sub>3</sub>  
 504 retrograde high-*P* granulite facies stage; (4) the subsequent (M<sub>4</sub> retrograde medium-*P* granulite  
 505 facies stage with peak *T* at ~860–900°C at 6 kbar; and (5) the later M<sub>5</sub> retrograde amphibolite facies  
 506 stage at <6.2 kbar *P* and ~710–730°C *T*. These *P*–*T* estimates define a clockwise *P*–*T* path  
 507 characterized by heating decompression from the *P*<sub>max</sub> stage of eclogite facies formation to the  
 508 *T*<sub>max</sub> stage for the granulite facies, followed by a final decompressional cooling stage to  
 509 amphibolite facies (Fig. 12).



510  
 511 **Figure 12.** The *P*–*T* path for the Nuomuhong eclogite in this study, compared with eclogite in the eastern  
 512 segment of the East Kunlun orogen from Song et al. (2018b). Boundaries for various metamorphic facies,  
 513 High-*P* granulite, UHT metamorphic facies according to Schreyer (1988), Syracuse et al. (2010), and  
 514 Maruyama et al. (1996). Abbreviations and phase equilibria are after Liou et al. (2004).



515

516 As already mentioned, the protoliths of the eclogite lithologies are interpreted to be subducted  
517 MORB-type oceanic crust, a fossil of the East Kunlun branch of the Proto-Tethys Ocean. The  
518 metamorphic change from M<sub>1</sub> prograde to M<sub>2</sub> peak-*P* eclogite facies at pressures of up to ~26 kbar,  
519 indicates that the oceanic crust was subducted down to ~83 km (Fig. 13A). This conclusion  
520 considers a lithostatic pressure of 1 kbar  $\approx$  3.2 km, where the eclogites underwent subduction zone  
521 *HP* metamorphism. The estimated *P*-*T* conditions for the peak-*P* stage Nuomuhong eclogites,  
522 corresponding to an apparent thermal gradient of ~220 °C/GPa, is a typical feature of generalized  
523 <375 °C/GPa low *T/P* geothermal subduction zones (Xia et al., 2022a). Locally, subduction of the  
524 oceanic crust under UHP condition resulted in the production of the coesite pseudomorphs recorded  
525 in the eastern EKOB rocks (Bi et al., 2018; Song et al., 2018b). Phase equilibrium modelling  
526 suggests that both the core and garnet rim minerals suggest a two phase increase in pressure and  
527 temperature conditions that ended with a reversed drop in pressure (Fig. 13C). The decompression  
528 process likely records a failed exhumation attempt that was followed by further burial, as  
529 demonstrated by the second segment of prograde evolution. In subduction channels, HP/UHP rock-  
530 bearing mélanges formed and evolved with different fates, including 1) successful exhumation to a  
531 shallow level accretionary complex, or 2) failed exhumation and subduction into the mantle.  
532 Multiple cycles of *P* increase during a single orogenic event, interpreted to represent burial-partial  
533 exhumation cycles, have been reported in eclogite from the Alps (Rubatto et al., 2011), western  
534 Dabie (Xia et al., 2022b) and the western Tianshan (Li et al., 2016) HP/UHP orogens. These cycles  
535 could have arisen because of convective flow in the subduction channel (Zheng et al., 2012).  
536 Therefore, M<sub>1</sub> and M<sub>2</sub> metamorphism of the Nuomuhong eclogites preserve thermal state history of

537 a Proto-Tethyan subduction zone and a complicated account of a Proto-Tethyan ocean crust  
538 subduction event during accretionary orogenesis.

539 The peak-*P* stage was followed by M<sub>3</sub> retrograde high-*P* granulite facies metamorphism and M<sub>4</sub>  
540 medium-*P* granulite facies, characterized by the symplectite Cpx II + Pl II rimming Cpx I<sub>b</sub>, and the  
541 symplectite Opx + Pl II rimming Cpx II. The calculated peak temperatures of ~860–900°C at ~6  
542 kbar indicate that eclogite was exhumed to the middle crust level, undergoing decompressional  
543 heating in the process. The high *T* metamorphic overprint on eclogite has not been recognized in  
544 other localities in the EKOB, implying that the Nuomuhong eclogite may have stayed in the middle  
545 crust for a sustained amount of time before final exhumation to the Earth surface. Such a situation  
546 was recently recognized in southern Tibet (Wang et al., 2021), where high-*T* overprinting of  
547 eclogite facies is regarded as metamorphic evidence of initial to mature stage continental collision.  
548 During the maturation of continental collision, the structural, magmatic, and metamorphic response  
549 changes significantly in the orogen. Firstly, the orogenic belt significantly thickens due to tectonic  
550 compression and continuous subduction of the down going continental lithosphere. Secondly, the  
551 subducting oceanic slab breaks off, leading to the buoyant exhumation of the deeply subducted  
552 continental crust to the middle-shallow level. In some circumstances, the change of geometry of  
553 orogenic wedges, experienced in mainly foreland basin sequences, accretionary and arc complexes,  
554 hampers the exhumation of HP/UHP rocks, resulting to persistence in the middle crust. In addition,  
555 slab break-off and crustal thinning promoted by upwelling of the asthenosphere, results in the  
556 eventual underplating of a large volume of mafic magma in the lower crust, leading to intense  
557 partial melting of crustal rocks and the generation of collision-related felsic magmatism. The  
558 underplating during collision-related magmatism acts as a potential heat source for the high-*T*

559 metamorphism that overprints previously exhumed HP/UHP metamorphic rocks (Fig. 13B).

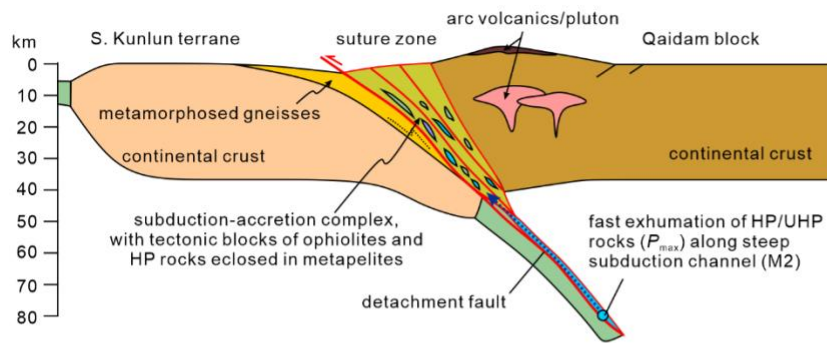
560 Therefore, the Nuomuhong eclogites preserve a long-term record for early subduction-accretionary  
561 to later collisional orogenesis.

562

### 563 **Implications for the evolution of the East Kunlun branch of the Proto-Tethys Ocean**

564 In the Qilian–Qaidam–Kunlun area along the northern margin of the Tibetan Plateau, several  
565 Early Paleozoic sutures separating microcontinental blocks and/or arc terranes were distributed  
566 between the northern Gondwana and combined Tarim–North China cratons, terminating in the  
567 ultimate closure of the Proto-Tethys Ocean (Fu et al., 2022a; Li et al., 2018c; Song et al., 2018a;  
568 Zhao et al., 2018). The remnants of the Proto-Tethys Ocean preserved in northern Tibet can be  
569 divided into the Qilian Ocean and North Qilian backarc in the north, the South Qilian Ocean in the  
570 middle, and the East Kunlun Ocean in the south, separated by the Central Qilan and Qaidam blocks  
571 (Fig. 13D), respectively (Song et al., 2018a). The detailed evolutionary history from continental  
572 rifting during the break of Rodinia, oceanic subduction-accretion, terrane accretion/collision and  
573 final continental collision, remains debated (Fu et al., 2019; Fu et al., 2018; Song et al., 2018b;  
574 Song et al., 2014; Wu et al., 2021; Wu et al., 2020; Wu et al., 2019; Xiao et al., 2009; Zuza et al.,  
575 2017). The EKOB contains complex geological units related to continental rifting, oceanic  
576 subduction and continental collision, providing an excellent window for evidencing the evolution of  
577 the Proto-Tethys Ocean and associated orogenesis (Song et al., 2018b).

**A) Initial collision with fast exhumation of HP/UHP rocks (ca. 430 Ma)**



**B) Mature collision with granulite facies overprinting (ca. 420 Ma)**

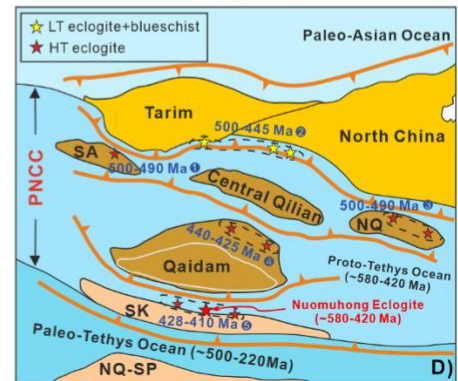
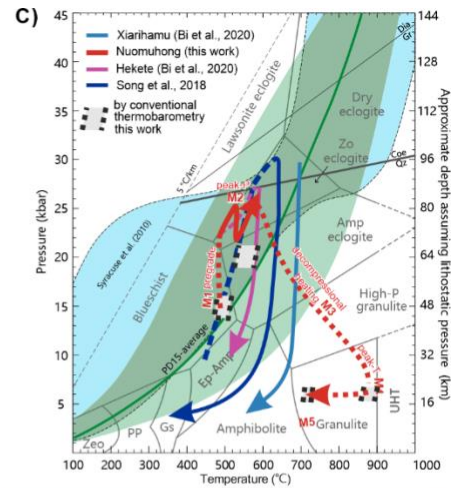
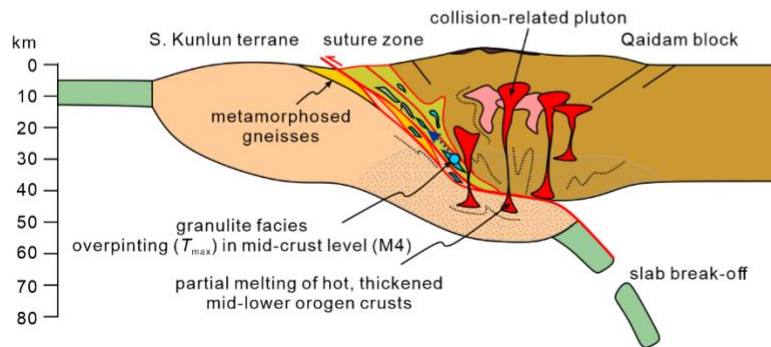


**Figure 13.** Tectonic model for the Eastern Kunlun orogen and the Proto-Tethys Ocean.

578

579

580

581

582

583

584

585

586

587

588

589

590

The continental rifting, supported by meta-gabbro in the south Jinshuikou Group in East Kunlun, yielded  $796 \pm 41$  Ma formation age (Ren et al., 2011). These data suggest that the East Kunlun began breaking up no later than  $796 \pm 41$  Ma, the Qingshuiquan ophiolite at  $522 \pm 4$  Ma and  $518 \pm 3$  Ma, the Tatuo ophiolite at  $522 \pm 3$  Ma, and the Buqingshan Delisitai MOR-ophiolite at  $516 \pm 6$  Ma (Liu et al., 2011b). The Early Paleozoic  $535 \pm 10$  Ma MOR-gabbro in the Maji Mountain area (Li, 2008), contains ample evidence for the formation of the East Kunlun oceanic crust (Lu et al., 2002; Yang et al., 1996). Subsequently, during the start of the late-Cambrian, the Kunlun Ocean began to subduct northward, with a series of magmatic and metamorphic events associated with this subduction event. The  $507 \pm 8$  Ma Qingshuiquan granulite in the central East Kunlun Suture zone and the  $480 \pm 3$  Ma Yaziquan island-arc diorite in the Qimantag Mountains (Cui et al., 2011; Li et al.,

591 2006), are an expression of these magmatic and metamorphic activities in the center and North  
592 Kunlun areas. Moreover, the time of formation of the  $515\pm 4$  Ma quartz diorite in the Kekesha area  
593 in Dulan, signifies the start of ocean basin subduction (Zhang et al., 2010b). During this time, the  
594 East Kunlun area stretched into several extensional oceanic or back-arc basins, as the oceanic crust  
595 was in a state of continuous expansion (Qi et al., 2016a).

596 From the late Ordovician to the early Silurian, the uninterrupted extension and distribution of  
597 back-arc basins in the Central East Kunlun zone continued with persistent and abundant magmatic  
598 activity (Chen et al., 2016). This conclusion is exemplified by the distribution of  $448\pm 4$  Ma  
599 basaltic-dacitic lavas near Central East Kunlun, including the deposition of the Bairiqiete  
600 intermediate acidic rock suite that formed island-arc granodiorites marked by the  $441\pm 6$  Ma and the  
601  $438\pm 3$  Ma island-arc rhyolite porphyry, the  $440\pm 6$  Ma Ykehalaer granodiorites of typical adakite  
602 geochemical characteristics (Li et al., 2014; Liu et al., 2011a), the  $447 \pm 9$  Ma metamorphosed  
603 diorite in the southern Xiangride area and the  $450\pm 4$  Ma rhyolite in the Nachita Group (Zhang et al.,  
604 2010c) . The diagenesis of arc magma occurred in response to oceanic crust subduction, while the  
605  $445\pm 5$  Ma SHRIMP ages for the Dagele ophiolite gabbro probably denote the ultimate subduction  
606 of the Proto-Tethys oceanic crust (Du et al., 2017).

607 After middle-late Silurian, final closure of the Kunlun branch of the Proto-Tethys Ocean,  
608 resulted into continental subduction and collisional orogeny. The high angle thrust nappe  
609 deformation in the East Kunlun Fault zone records a 426–408 Ma age for this event (Wang et al.,  
610 2003b), and marks the disappearance of the island arc environment alongside contemporaneous  
611 early Paleozoic collisional orogenic activity. There are a great deal of medium-late Silurian to early  
612 Devonian collisional granites (Li et al., 2013; Liu et al., 2012). These granites are typified by the

613 425±7 Ma Helegangnaren A-type alkali feldspar granite, the 407±3 Ma Yuejinshan granodiorite, the  
614 423±5 Ma syn-collisional granite from the Changshishan mélangé belt, distributed between the  
615 north Kunlun and the southern margin of the Qaidam block. Collectively, these lithologies are  
616 identical with this tectonic environment, while the presence of the 428–411 Ma Nuomuhong  
617 eclogite and others in the East Kunlun record the ensuing continental subduction and collisional  
618 orogeny.

619 We propose that when the Kunlun Ocean crust subducted towards the north and under the  
620 southern margin of the Qaidam Block during the Early Paleozoic before 440 Ma, the continental  
621 basaltic protolith of the East Kunlun eclogites formed in a continental margin setting, were  
622 impacted by oceanic crust subduction. The high-amphibolite to granulite facies metamorphism  
623 owing to tecto-thermal events of oceanic crust subduction, is associated with the prograde minerals  
624 assemblage of the Nuomuhong eclogites and the 460 Ma Jinshuikou Group gneissic lithologies  
625 (Zhang et al., 2003). After the early Silurian continental subduction and collisional orogeny closure  
626 of the Proto-Tethys Ocean, the protolith of the Jinshuikou Group basement mafic rocks were buried  
627 down to >100 km depth in the subduction channel. Evidence of HP-UHP metamorphism, in  
628 addition to the eclogite facies, is supported by the intercalation of the country rocks with eclogites  
629 (Bi et al., 2020).

630 When the East Kunlun orogenic belt began its post-collisional extension in the middle-late  
631 Silurian, the eclogites were exhumed onto the shallow crust. The slight 430–411 Ma timing gap for  
632 the accumulation of these eclogites in East Kunlun (Meng et al., 2013b; Qi et al., 2014; Qi et al.,  
633 2016a; Song et al., 2018b), is probably attributed to uneven timing and speed of exhumation in  
634 different parts of the enormous orogenic belt, accompanied by internal asymmetric subduction

635 suturing (Bi et al., 2022), evidenced by eclogites in the eastern and western Kunlun outcrops.  
636 Eventually the molasse sedimentary assemblage of the Devonian Maoniushan group signified the  
637 end of the early Paleozoic Proto-Tethys Ocean tectonic cycle in East Kunlun and the beginning of  
638 the new cycle of ocean-continental evolution associated with the North Paleo-Tethys Ocean (Chen  
639 et al., 2008b; Li et al., 2013).

640 The discovery of the Nuomuhong eclogite constrained the timing of transition from continental  
641 subduction to collision in the early Devonian and formed a super HP-UHP metamorphic belt with  
642 other eclogite outcrops in the EKOB block. This assemblage represents an excellent example of an  
643 early Paleozoic continental convergence boundary between the Qaidam Block and the East Kunlun  
644 Massif, which is of great significance for furthering the understanding, formation, and evolution of  
645 the Proto-Tethys system.

646

## 647 CONCLUSION

648 (1) Retrograde eclogites with garnet and omphacite formed during partial tectonic  
649 decompression, characterizes the Nuomuhong area in the eastern part of the East Kunlun orogenic  
650 belt. The retrograde eclogites underwent prograde, eclogite, HP granulite, granulite, and  
651 amphibolite facies metamorphisms, along a  $P$ - $T$  clockwise pathway: (1) the M1 prograde stage with  
652  $P$ - $T$  conditions of  $>14.0$  kbar/ $\sim 470$ – $506^\circ\text{C}$ ; (2) the peak- $P$  eclogite facies stage (M2,  $\sim 26$   
653 kbar/ $\sim 570^\circ\text{C}$ ); (3) the early retrograde high- $P$  granulite facies stage (M3); (4) the subsequent  
654 retrograde high- $T$  granulite facies stage (M4) with peak  $T$  at  $\sim 860$ – $900^\circ\text{C}$  at a pressure of 6 kbar;  
655 and (5) the later retrograde amphibolite facies stage (M5,  $< 6.2$  kbar/ $\sim 710$ – $730^\circ\text{C}$ ). The  
656 orthopyroxene associated with eclogite in EKOB revealed that the Nuomuhong eclogites

657 experienced granulite metamorphism different from the other eclogites in EKOB.

658 (2) The protolith of the Nuomuhong eclogite with slight LREE enrichment has MOR basalt-like  
659 geochemical signatures. Zircon U–Pb analyses and Raman spectrometer show the peak  
660 metamorphism or early exhumation formed at  $419 \pm 4$  Ma (MSWD=1.3). The zircon cores ages  
661 yielding  $464 \pm 4$  Ma (MSWD=0.5) recorded the protolith ages of Nuomuhong eclogite rather than  
662 the Middle Ordovician tectonic-thermal events associating with the metamorphic ages of Jinshuikou  
663 Group.

664 (3) The oceanic crust of East Kunlun Ocean, the southern part of Proto-Tethys Ocean, formed  
665 before the middle Cambrian and began to subduct northward after initial late-Cambrian. From the  
666 late Ordovician to the early Silurian, the back-arc basins distributing along the Central East Kunlun  
667 continued extending with abundant magmatic activities. After middle-late Silurian, the Kunlun  
668 Ocean, a branch of Proto-Tethys Ocean, had closed finally and transformed into the continental  
669 subduction and collisional orogeny. The presence of Nuomuhong eclogite and other eclogites (~~428–~~  
670 ~~411 Ma~~) in East Kunlun also recorded the continental subduction and collisional orogeny. Finally,  
671 the later Devonian molasse sedimentary assemblage represented the end of the Proto-Tethys  
672 evolution and the beginning of Paleo-Tethys evolution in East Kunlun. The discovery of  
673 Nuomuhong eclogite formed a HP-UHP metamorphism belt with other eclogite dew points in East  
674 Kunlun.

675

## 676 **ACKNOWLEDGEMENTS**

677 Financial support for this study was jointly provided by the National Natural Science  
678 Foundation of China (Grant No. 41703024, 42102244, 4210268), the China Geological Survey



679 Project (Grant No. 1212010510507 and DD20221814) and the China Scholarship Council (Grant  
680 No. 201906415032). We give our thanks to Profs. Tim Kusky and Lu Wang for their constructive  
681 suggestions and helpful comments to improve this manuscript.

682

683 **REFERENCES**

- 684 Bi, H., Song, S., Dong, J., Yang, L., Qi, S., and Allen, M. B., 2018, First discovery of coesite in eclogite from East Kunlun,  
685 northwest China: *Science Bulletin*, v. 63, no. 23, p. 1536-1538.
- 686 Bi, H., Whitney, D., Song, S., and Zhou, X., 2022, HP–UHP eclogites in the East Kunlun Orogen, China: P–T evidence for  
687 asymmetric suturing of the Proto-Tethys Ocean: *Gondwana Research*, v. 104, p. 199-214.
- 688 Bi, H. Z., Song, S. G., Yang, L. M., Allen, M. B., Qi, S. S., and Su, L., 2020, UHP metamorphism recorded by coesite-  
689 bearing metapelite in the East Kunlun Orogen (NW China): *Geological Magazine*, v. 157, no. 2, p. 160-172.
- 690 Bingen, B., Davis, W. J., and Austrheim, H., 2001, Zircon U-Pb geochronology in the Bergen arc eclogites and their  
691 Proterozoic protoliths, and implications for the pre-Scandian evolution of the Caledonides in western Norway:  
692 *Geological Society of America Bulletin*, v. 113, no. 5, p. 640-649.
- 693 Cabanis, B., and Lecolle, M., 1989, Le diagramme La/10Y/15Nb/8: un outil pour la discrimination des sries volcaniques  
694 et la mise en vidence des procsses de mlanges et/ou de contamination crus-tale: *CR Acad. Sci., Sr*, v. 2, p. 2023-  
695 2029.
- 696 Chen, J. J., Fu, L. B., Wei, J. H., Tian, N., Xiong, L., Zhao, Y. J., and Qi, Y. Q., 2016, Geochemical characteristics of Late  
697 Ordovician granodiorite in Gouli Area, Eastern Kunlun Orogenic Belt, Qinghai Province: Implications on the  
698 Evolution of Proto-Tetys Ocean.: *Earth Science*, v. 41, no. 11, p. 1863-1882.
- 699 Chen, N., Sun, M., Wang, Q., Zhang, K., Wan, Y., and Chen, H., 2008a, U-Pb dating of zircon from the Central Zone of  
700 the East Kunlun Orogen and its implications for tectonic evolution: *Science in China Series D: Earth Sciences*, v.  
701 51, no. 7, p. 929-938.
- 702 Chen, N. S., Sun, M., Wang, Q. Y., Zhang, K. X., Wan, Y. S., and Chen, H. H., 2008b, Zircon U-Pb dating and tectonic  
703 evolution implications in the central belt of East Kunlun Orogenic Belt *SCIENCE CHINA Earth Sciences*, v. 38, no.  
704 6, p. 657-666.

705 Chen, X., Xu, R. K., Zheng, Y. Y., Wang, Y. K., Wang, H. J., Bai, J., Du, W. Y., and Lu, R., 2015, The determination of peak  
706 temperature of eclogites in the west of Tieshiguan area, North Qaidam UHP of Qinghai Province, and its  
707 geological significance: *Geological Bulletin of China*, v. 34, no. 12, p. 2292-2301.

708 Chen, Y. X., Pei, X. Z., Li, R. B., Liu, Z. Q., Li, Z. C., Zhang, X. F., Chen, G. C., Liu, Z. G., Ding, S., and Guo, J., 2011, Zircon U-  
709 Pb Age of Xiaomiao Formation of Proterozoic in the Eastern Section of the East Kunlun Orogenic Belt:  
710 *GEOSCIENCE*, v. 25, no. 3, p. 510-521.

711 Coleman, R. G., Lee, D. E., Beatty, L. B., and Brannock, W. W., 1965, Eclogites and Eclogites: Their Differences and  
712 Similarities: *Geological Society of America Bulletin*, v. 76, no. 5, p. 483.

713 Corfu, F., Hanchar, J. M., Hoskin, P. W. O., and Kinny, P., 2003, Atlas of Zircon Textures: Reviews in Mineralogy and  
714 Geochemistry, v. 53, no. 1, p. 469–500.

715 Cui, M. H., Meng, F. C., and Wu, X. K., 2011, Early Ordovician island arc of Yaziquan, west of Qimantag Mountain, East  
716 Kunlun: evidences from geochemistry, Sm-Nd isotope and geochronology of intermediate-basic rocks: *Acta  
717 Petrologica Sinica* v. 27, no. 11, p. 3365-3379.

718 Dobretsov, N. L., 1991, Blueschists and eclogites: a possible plate tectonic mechanism for their emplacement from the  
719 upper mantle: *Tectonophysics*, v. 186, no. 3-4, p. 253–268.

720 Dong, Y. P., He, D. F., Sun, S. S., Liu, X. M., Zhou, X. H., Zhang, F. F., Yang, Z., Cheng, B., Zhao, G. C., and Li, J. H., 2018,  
721 Subduction and accretionary tectonics of the East Kunlun orogen, western segment of the Central China  
722 Orogenic System: *Earth-Science Reviews*, v. 186, p. 231-261.

723 Du, W., Jiang, C., Xia, M., Xia, Z., Zhou, W., Ling, J., Wang, B., and Yu, S., 2017, A newly discovered Early Paleozoic  
724 ophiolite in Dagele, Eastern Kunlun, China, and its geological significance: *Geological Journal*, v. 52, p. 425-435.

725 Feng, D., Wang, C., Song, S., Xiong, L., Zhang, G., Allen, M. B., Dong, J., Wen, T., and Su, L., 2023, Tracing tectonic  
726 processes from Proto- to Paleo-Tethys in the East Kunlun Orogen by detrital zircons: *Gondwana Research*, v.

727 115, p. 1-16.

728 Fu, C. L., Yan, Z., Guo, X. Q., Niu, M. L., Cao, B., Wu, Q., Li, X., and Wang, Z. Q., 2019, Assembly and dispersal history of  
729 continental blocks within the Altun-Qilian-North Qaidam mountain belt, NW China: *International Geology*  
730 *Review*, v. 61, no. 4, p. 424-447.

731 Fu, D., Huang, B., Johnson, T. E., Wilde, S. A., Jourdan, F., Polat, A., Windley, B. F., Hu, Z., and Kusky, T., 2022a, Boninitic  
732 blueschists record subduction initiation and subsequent accretion of an arc–forearc in the northeast Proto-  
733 Tethys Ocean: *Geology*, v. 50, no. 1, p. 10-15.

734 Fu, D., Kusky, T., Wilde, S. A., Polat, A., Huang, B., and Zhou, Z., 2018, Early Paleozoic collision-related magmatism in the  
735 eastern North Qilian orogen, northern Tibet: A linkage between accretionary and collisional orogenesis: *GSA*  
736 *Bulletin*, v. 131, no. 5-6, p. 1031-1056.

737 Fu, L., Bagas, L., Wei, J., Chen, Y., Chen, J., Zhao, X., Zhao, Z., Li, A., and Zhang, W., 2022b, Growth of early Paleozoic  
738 continental crust linked to the Proto-Tethys subduction and continental collision in the East Kunlun Orogen,  
739 northern Tibetan Plateau: *GSA Bulletin*.

740 Green, E. C. R., White, R. W., Diener, J. F. A., Powell, R., Holland, T. J. B., and Palin, R. M., 2016, Activity-composition  
741 relations for the calculation of partial melting equilibria in metabasic rocks: *Journal of Metamorphic Geology*,  
742 v. 34, no. 9, p. 845-869.

743 Guo, F., Wang, P., Wang, Z., and Feng, N., 2020, Geochemical and geochronology characteristics of retrograde eclogite  
744 in Xiarihamu area, East Kunlun Mountains, and its geological implications: *Sedimentary Geology and Tethyan*  
745 *Geology*, v. 40, no. 4, p. 45-55.

746 Han, L., Zhang, L., and Zhang, G., 2015, Ultra-deep subduction of Yematan eclogite in the North Qaidam UHP belt, NW  
747 China: Evidence from phengite exsolution in omphacite: *American Mineralogist*, v. 100, no. 8-9, p. 1848-1855.

748 He, D. F., Dong, Y. P., Liu, X. M., Yang, Z., Sun, S. S., Cheng, B., and Li, W., 2016, Tectono-thermal events in East Kunlun,

749 Northern Tibetan Plateau: Evidence from zircon U–Pb geochronology: *Gondwana Research*, v. 30, p. 179-190.

750 Hermann, J., 2002, Allanite: Thorium and light rare earth element carrier in subducted crust: *Chemical Geology*, v. 192,  
751 no. 3, p. 289-306.

752 Hertgen, S., Yamato, P., Morales, L., and Angiboust, S., Brittle/Ductile deformation at depth during continental crust  
753 eclogitization (Mont-Emilius klippe, Western Internal Alps), *in* Proceedings EGU General Assembly  
754 Conference2016, Volume 18.

755 Holland, T., and Blundy, J., 1994, Non-ideal interactions in calcic amphiboles and their bearing on amphibole-  
756 plagioclase thermometry: *Contributions to Mineralogy and Petrology*, v. 116, no. 4, p. 433-447.

757 Holland, T. J. B., and Powell, R., 2011, An improved and extended internally consistent thermodynamic dataset for  
758 phases of petrological interest, involving a new equation of state for solids: *Journal of metamorphic Geology*, v.  
759 29, no. 3, p. 333-383.

760 Irvine, T. N., and Baragar, W. R. A., 1971, A Guide to the Chemical Classification of the Common Volcanic Rocks:  
761 *Canadian Journal of Earth Sciences*, v. 8, no. 5, p. 523-548.

762 Jia, L. H., Meng, F. C., and Feng, H. B., 2014, Fluid activity during eclogite-facies peak metamorphism: Evidence from a  
763 quartz vein in eclogite in the East Kunlun, NW China: *Acta Petrologica Sinica*, v. 30, no. 8, p. 2339-2350.

764 Jiang, C. F., Yang, J. S., Feng, B. G., Zhu, Z. Z., Zhao, M., Chai, Y. C., Shi, X. D., Wang, H. D., and Hu, J. Q., 1992, Opening-  
765 Closing Tectonics of Kunlun Mountains, Beijing, Geological Publishing House Geol. Memo. Series 5.

766 Klonowska, I., Janák, M., Majka, J., Froitzheim, N., and Kościńska, K., 2016, Eclogite and garnet pyroxenite from Stor  
767 Jougdan, Seve Nappe Complex, Sweden: implications for UHP metamorphism of allochthons in the  
768 Scandinavian Caledonides: *Journal of Metamorphic Geology*, v. 34, no. 2, p. 103-119.

769 Leake, B. E., Woolley, A. R., Arps, C. E., Birch, W. D., Gilbert, M. C., Grice, J. D., Hawthorne, F. C., Kato, A., Kisch, H. J.,  
770 and Krivovichev, V. G., 1997, Nomenclature of amphiboles; report of the Subcommittee on Amphiboles of the

771 International Mineralogical Association Commission on new minerals and mineral names: Mineralogical  
772 magazine, v. 61, no. 405, p. 295-310.

773 Leake, B. E., Woolley, A. R., Birch, W. D., Burke, E. A., Ferraris, G., Grice, J. D., Hawthorne, F. C., Kisch, H. J., Krivovichev,  
774 V. G., and Schumacher, J. C., 2004, Nomenclature of amphiboles: additions and revisions to the International  
775 Mineralogical Association's amphibole nomenclature: Mineralogical Magazine, v. 68, no. 1, p. 209-215.

776 Li, B. S., Yan, M. D., Zhang, W. L., Fang, X. M., Yang, Y. P., Zhang, D. W., Chen, Y., and Guan, C., 2018a, Paleomagnetic  
777 Rotation Constraints on the Deformation of the Northern Qaidam Marginal Thrust Belt and Implications for  
778 Strike-Slip Faulting Along the Altyn Tagh Fault: Journal of Geophysical Research: Solid Earth, v. 123, no. 9, p.  
779 7207-7224.

780 Li, H. K., Lu, S. N., Xiang, Z. Q., Zhou, H. Y., Guo, H., Song, B., Zheng, J. K., and Gu, Y., 2006, SHRIMP U-Pb zircon age of  
781 the granulite from the Qingshuiquan area, Central Eastern Kunlun Suture Zone: Earth Science Frontiers, v. 13,  
782 no. 6, p. 311-321.

783 Li, J., Gao, J., and Wang, X., 2016, A subduction channel model for exhumation of oceanic-type high-pressure to  
784 ultrahigh-pressure eclogite-facies metamorphic rocks in SW Tianshan, China: Science China Earth Sciences, v.  
785 59, no. 12, p. 2339-2354.

786 Li, R. B., Pei, X. Z., Li, Z. C., Chen, G. C., Liu, C. J., Chen, Y. X., Liu, Z. Q., and Pei, L., 2014, Age, Geochemical  
787 Characteristics and Tectonic Significance of Yikehalaer Granodiorite in Buqingshan Tectonic Mélange Belt,  
788 Southern Margin of East Kunlun: Acta Geoscientia Sinica, v. 4, p. 434-444.

789 Li, R. B., Pei, X. Z., Li, Z. C., Pei, L., Chen, G. C., Wei, B., Chen, Y. X., Liu, C. J., and Wang, M., 2018b, Cambrian (~ 510 Ma)  
790 ophiolites of the East Kunlun orogen, China: A case study from the Acite ophiolitic tectonic mélange:  
791 International Geology Review, v. 60, no. 16, p. 2063-2083.

792 Li, R. B., Pei, X. Z., Li, Z. C., Sun, Y., Pei, L., Chen, G. C., Chen, Y. X., Liu, C. J., and Wei, F. H., 2013, Regional Tectonic

793 Transformation in East Kunlun Orogenic Belt in Early Paleozoic: Constraints from the Geochronology and  
794 Geochemistry of Helegangnaren Alkali-feldspar Granite: ACTA GEOLOGICA SINICA English Edition, v. 87, no. 2,  
795 p. 333-345.

796 Li, S. Z., Zhao, S. J., Liu, X., Cao, H. H., Yu, S., Li, X. Y., Somerville, I., Yu, S. Y., and Suo, Y. H., 2018c, Closure of the Proto-  
797 Tethys Ocean and Early Paleozoic amalgamation of microcontinental blocks in East Asia: Earth-Science  
798 Reviews, v. 186, p. 37-75.

799 Li, W. Y., 2008, Chronology and Geochemistry of ophiolite and Island arc magmatic rocks in West Qingling-East Kunlun  
800 Orogenic Belt, Constraint for Tethys evolution [doctor: University of Science and Technology of China, 1-154 p.

801 Liou, J. G., Tsujimori, T., Zhang, R. Y., Katayama, I., and Maruyama, S., 2004, Global UHP Metamorphism and  
802 Continental Subduction/Collision: The Himalayan Model: International Geology Review, v. 46, no. 1, p. 1-27.

803 Liu, B., Ma, C. Q., Zhang, J. Y., Xiong, F. H., Huang, J., and Jiang, H. A., 2012, Petrogenesis of Early Devonian intrusive  
804 rocks in the east part of Eastern Kunlun Orogen and implication for Early Palaeozoic orogenic processes: Acta  
805 Petrologica Sinica, no. 6, p. 1785-1807.

806 Liu, Q., Meng, F., Li, S., Feng, H., Jia, L., and Tian, G., 2016, Geochronology of zircon from the paragneiss of Kuhai Group  
807 in southern East Kunlun terrane: ACTA PETROLOGICA ET MINERALOGICA, v. 35, no. 3, p. 15.

808 Liu, Z. Q., Pei, X. Z., Li, R. B., Li, Z. C., Chen, G. C., Chen, Y. X., Gao, J. M., Liu, C. J., Wei, F. H., Wang, X. L., and Zhang, G.,  
809 2011a, Early Paleozoic intermediate-acid magmatic activity in Bairiqiete area along the Buqingshan tectonic  
810 melange belt on the southern margin of East Kunlun: Constraints from zircon U-Pb dating and geochemistry:  
811 Geology in China, v. 38, no. 5, p. 1150-1167.

812 Liu, Z. Q., Pei, X. Z., Li, R. B., Li, Z. C., Zhang, X. F., Liu, Z. G., Chen, Y. X., Chen, G. C., Ding, S. P., and Guo, J. F., 2011b, LA-  
813 ICP-MS Zircon U-Pb Geochronology of the Two Suites of Ophiolites at the Buqingshan Area of the A'nyemaqen  
814 Orogenic Belt in the Southern Margin of East Kunlun and its Tectonic Implication: ACTA GEOLOGICA SINICA, v.

815 85, no. 2, p. 185-194.

816 Lu, L., Wu, H. Z., Hu, D. G., BAROSH, P. J., Hao, S., and C.J., Z., 2010, Zircon U-Pb age for rhyolite of the Maoniushan  
817 Formation and its tectonic significance in the East Kunlun Mountains: *Acta Petrologica Sinica*, v. 26, no. 4, p.  
818 1150-1158.

819 Lu, S. N., Yu, H. F., Jin, W., Li, H. K., and Zheng, J. K., 2002, Microcontinents on the eastern margin of Tarim  
820 paleocontinent: *Acta Petrologica et Mineralogica*, v. 21, no. 4, p. 317-326.

821 Luo, Z. H., Deng, J. F., Cao, Y. Q., Guo, Z. F., and Mo, X. X., 1999, On Late Paleozoic-Early Mesozoic volcanism and  
822 regional tectonic evolution of eastern Kunlun, Qinghai Province: *Geoscience*, v. 13, no. 1, p. 51-56.

823 Maruyama, S., Liou, J., and Terabayashi, M. J. I. g. r., 1996, Blueschists and eclogites of the world and their exhumation,  
824 v. 38, no. 6, p. 485-594.

825 Meng, F., Cui, M., Wu, X., Wu, J., and Wang, J., 2013a, Magmatic and metamorphic events recorded in granitic gneisses  
826 from the Qimantag, East Kunlun Mountains, Northwest China: *Acta Petrologica Sinica*, v. 29, no. 6, p. 2107-  
827 2122.

828 Meng, F. C., Cui, M. H., Jia, L. H., Ren, Y. F., and Feng, H. B., 2015a, Paleozoic continental collision of the East Kunlun  
829 orogen: Evidence from protoliths of the eclogites: *Acta Petrologica Sinica*, v. 31, no. 12, p. 3581-3594.

830 Meng, F. C., Cui, M. H., Wu, X. K., and Ren, Y. F., 2015b, Heishan mafic-ultramafic rocks in the Qimantag area of Eastern  
831 Kunlun, NW China: Remnants of an early Paleozoic incipient island arc: *Gondwana Research*, v. 27, no. 2, p.  
832 745-759.

833 Meng, F. C., Jia, L. H., Ren, Y. F., Liu, Q., and Duan, X. P., 2017, Magmatic and metamorphic events recorded in the  
834 gneisses of the Wenquan region, East Kunlun Mountains, Northwest China: Evidence from the zircon U-Pb  
835 geochronology: *Acta Petrologica Sinica*, v. 33, no. 12, p. 3691-3709.

836 Meng, F. C., Tian, G., Duan, X. P., Fan, Y., and Ren, Y., 2018, Evidence from Garnet for Genesis of Garnet-Cordierite-



837 Granite in the Jinshuikou Area, Eastern Segment of the East Kunlun Mountains: *Bulletin of Mineralogy,*  
838 *Petrology Geochemistry* v. 37, no. 2, p. 192-204.

839 Meng, F. C., Yang, H. J., Makeyev, A. B., Ren, Y. F., Kulikova, K. V., and Bryanchaninova, N. I., 2016, Jadeitite in the Syum-  
840 Keu ultramafic complex from Polar Urals, Russia: insights into fluid activity in subduction zones: *European*  
841 *Journal of Mineralogy*, v. 28, no. 6, p. 1079-1097.

842 Meng, F. C., Zhang, J. X., and Cui, M. H., 2013b, Discovery of Early Paleozoic eclogite from the East Kunlun, Western  
843 China and its tectonic significance: *Gondwana Research*, v. 23, no. 2, p. 825-836.

844 Meschede, M., 1986, A method of discriminating between different types of mid-ocean ridge basalts and continental  
845 tholeiites with the Nb · 1bZr · 1bY diagram: *Chemical geology*, v. 56, no. 3-4, p. 207-218.

846 Mo, X. X., Luo, Z. H., Deng, J. F., Yu, X. H., Liu, C. D., Chen, H. W., and Liu, H. Y., 2007, Granitoids and Crustal Growth in  
847 the East Kunlun Orogenic Belt: *Geological Journal of China Universities*, v. 13, no. 3, p. 403-414.

848 Morimoto, N., 1988, Nomenclature of pyroxenes: *Mineralogy & Petrology*, v. 39, no. 1, p. 55-76.

849 Pan, T., and Zhang, Y., 2020, Geochemical Characteristics and Metallogenic Response of the Eclogite from Xiarihamu  
850 Magmatic Ni-Cu Sulfide Deposit in Eastern Kunlun Orogenic Belt: *Geotectonica et Metallogenia*, v. 44, no. 3, p.  
851 447-464.

852 Pearce, J. A., 1982, Trace element characteristics of lavas from destructive plate boundaries, *in* Thorpe, R. S., ed.,  
853 *Andesites: Orogenic Andesites and Related Rocks*: Chichester, England, John Wiley & Sons, p. 528-548.

854 Pearce, J. A., and Norry, M. J., 1979, Petrogenetic implications of Ti, Zr, Y, and Nb variations in volcanic rocks:  
855 *Contributions to Mineralogy & Petrology*, v. 69, no. 1, p. 33-47.

856 Qi, S. S., Song, S. G., Shi, L. C., Cai, H. J., and Hu, J. C., 2014, Discovery and its geological significance of Early Paleozoic  
857 eclogite in Xiarihamu-Suhaitu area, western part of the East Kunlun: *Acta Petrologica Sinica*, v. 30, no. 11, p.  
858 3345-3356.

859 Qi, X. P., Fan, X. G., Yang, J., Cui, J. T., Wang, B. Y., and Fan, Y. Z., 2016a, The discovery of Early Paleozoic eclogite in the  
860 upper reaches of Langmuri in eastern East Kunlun Mountains and its significance: Geological Bulletin of China,  
861 v. 35, no. 11, p. 1771-1783.

862 Qi, X. P., Fan, X. G., Yang, J., Cui, J. T., Wang, B. Y., and Fan, Y. Z., 2016b, The discovery of Early Paleozoic eclogite in the  
863 upper reaches of Langmuri in eastern East Kunlun Mountains and its significance: Geological Bulletin of China,  
864 v. 35, no. 11, p. 1771-1783.

865 Qi, X. P., Yang, J., Fan, X. G., Cui, J. T., Cai, Z. F., Zeng, X. W., Wei, W., Qu, X. X., and Zhai, Y. M., 2016c, Age, geochemical  
866 characteristics and tectonic significance of Changshishan ophiolite in central East Kunlun tectonic mélange  
867 belt along the east section of East Kunlun Mountains: Geology in China, v. 43, no. 3, p. 797--816.

868 Ravna, K., 2000, The garnet–clinopyroxene Fe<sup>2+</sup>–Mg geothermometer: an updated calibration: Journal of  
869 Metamorphic Geology, v. 18, no. 2, p. 211-219.

870 Ren, J. H., Zhang, K., Liu, Y. Q., Zhou, D. W., and Feng, Q., 2011, Geochemical characteristics and zircon dating of blasto-  
871 gabro from the South Jinshuikou area, Eastern Kunlun: JOURNAL OF NORTHWEST UNIVERSITY(NATURAL  
872 SCIENCE EDITION), v. 41, no. 1, p. 100-106.

873 Rubatto, D., Regis, D., Hermann, J., Boston, K., Engi, M., Beltrando, M., and McAlpine, S. R. B., 2011, Yo-yo subduction  
874 recorded by accessory minerals in the Italian Western Alps: Nature Geoscience, v. 4, no. 5, p. 338-342.

875 Sajeev, K., Windley, B. F., Hegner, E., and Komiya, T., 2013, High-temperature, high-pressure granulites (retrogressed  
876 eclogites) in the central region of the Lewisian, NW Scotland: Crustal-scale subduction in the Neoproterozoic:  
877 Gondwana Research, v. 23, no. 2, p. 526-538.

878 Schmidt, M. W., 1992, Amphibole composition in tonalite as a function of pressure: an experimental calibration of the  
879 Al-in-hornblende barometer: Contributions to Mineralogy&Petrology, v. 110, no. 2, p. 304-310.

880 Schorn, S., and Diener, J. F. A., 2017, Details of the gabbro-to-eclogite transition determined from microtextures and

881 calculated chemical potential relationships: *Journal of Metamorphic Geology*, v. 35, no. 1, p. 55-75.

882 Schreyer, W., 1988, Experimental studies on metamorphism of crustal rocks under mantle pressures: *Mineralogical*  
883 *Magazine*, v. 52, no. 364, p. 1-26.

884 Şengör, A. M. C., 1984, The Cimmeride Orogenic System and the Tectonics of Eurasia, *The Cimmeride Orogenic System*  
885 *and the Tectonics of Eurasia*, Volume 195, Geological Society of America, p. 0.

886 Smith, D. C., 1984, Coesite in clinopyroxene in the Caledonides and its implications for geodynamics: *Nature*, v. 310, no.  
887 5979, p. 641-644.

888 Smith, J. V., 1974, *Chemical and textural properties*, Berlin Heidelberg New York, Springer, Feldspar minerals.

889 Sobolev, N. V., Dobretsov, N. L., Bakirov, A. B., and Shatsky, V. S., 1986, Eclogites from various types of metamorphic  
890 complexes in the USSR and the problems of their origin: *Geological Society of America Memoirs*, p. 349-364.

891 Song, S., Niu, Y., Zhang, G., and Zhang, L., 2018a, Two epochs of eclogite metamorphism link 'cold' oceanic subduction  
892 and 'hot' continental subduction, the North Qaidam UHP belt, NW China: *Geological Society of London*, v. 474,  
893 p. 1-15.

894 Song, S. G., Bi, H. Z., Qi, S. S., Yang, L. M., Allen, M. B., Niu, Y. L., Su, L., and Li, W. F., 2018b, HP–UHP Metamorphic Belt  
895 in the East Kunlun Orogen: Final Closure of the Proto-Tethys Ocean and Formation of the Pan-North-China  
896 Continent: *Journal of Petrology*, v. 59, no. 11, p. 2043-2060.

897 Song, S. G., Niu, Y. L., Su, L., Zhang, C., and Zhang, L. F., 2014, Continental orogenesis from ocean subduction, continent  
898 collision/subduction, to orogen collapse, and orogen recycling: The example of the North Qaidam UHPM belt,  
899 NW China: *Earth-Science Reviews*, v. 129, p. 59-84.

900 Song, S. G., Su, L., Li, X. H., Niu, Y. L., and Zhang, L. f., 2012, Grenville-age orogenesis in the Qaidam-Qilian block: the  
901 link between South China and Tarim: *Precambrian Research*, v. 220, p. 9-22.

902 Song, S. G., Zhang, I. F., Wei, C. J., Liou, J. G., and Sun, G. M., 2007, Eclogite and carpholite - bearing metasedimentary

903 rocks in the North Qilian suture zone, NW China: implications for Early Palaeozoic cold oceanic subduction  
904 and water transport into mantle *Journal of Metamorphic Geology*, v. 25, no. 5, p. 547-563.

905 Sun, J., Dong, Y., Ma, L., Chen, S., and Jiang, W., 2022, Devonian to Triassic tectonic evolution and basin transition in the  
906 East Kunlun–Qaidam area, northern Tibetan Plateau: Constraints from stratigraphy and detrital zircon U–Pb  
907 geochronology: *GSA Bulletin*, v. 134, no. 7-8, p. 1967-1993.

908 Sun, S. S., and McDonough, W. F., 1989, Chemical and isotopic systematic of Oceanic basalt: Implications for the  
909 mantle composition and processes, Geological Society, London, Special Publications, 313-345 p.:

910 Syracuse, E. M., van Keken, P. E., and Abers, G. A., 2010, The global range of subduction zone thermal models: *Physics  
911 of the Earth and Planetary Interiors*, v. 183, no. 1, p. 73-90.

912 Tang, H., Zhang, H. F., Zhang, M. J., Zou, H., and Zhang, J., 2022, Neoproterozoic and early Paleozoic metamorphism  
913 recorded in gneisses from the East Kunlun Orogenic belt: *Precambrian Research*, v. 375.

914 Wang, B. Z., Luo, Z. H., Pan, T., Song, T. Z., Xiao, P. X., and Zhang, Z. Q., 2012, Petrotectonic assemblages and LA-ICP-MS  
915 zircon U-Pb age of Early Paleozoic volcanic rocks in Qimantag area, Tibetan Plateau: *Geological Bulletin of  
916 China*, v. 31, no. 6, p. 860-874.

917 Wang, G., Chen, N., Zhu, Y., and Zhang, K., 2003a, Late Caledonian Ductile Thrusting Deformation in the Central East  
918 Kunlun Belt, Qinghai, China and Its Significance: Evidence from Geochronology: *Acta Geologica Sinica - English  
919 Edition*, v. 77, no. 3, p. 311-319.

920 Wang, G., Chen, N., Zhu, Y., and Zhang, K., 2003b, Late Caledonian Ductile Thrusting Deformation in the Central East  
921 Kunlun Belt, Qinghai, China and Its Significance: Evidence from Geochronology: *Acta Geologica Sinica*, v. 77,  
922 no. 3, p. 311-319.

923 Wang, H., Wu, Y., Gao, S., Liu, X., Liu, Q., Qin, Z., Xie, S., Zhou, L., and Yang, S., 2013a, Continental origin of eclogites in  
924 the North Qinling terrane and its tectonic implications: *Precambrian Research*, v. 230, no. Complete, p. 13-30.

925 Wang, H., Xiao, W., Windley, B. F., Zhang, Q. W. L., Tan, Z., Wu, C., and Shi, M., 2022a, Diverse P-T-t Paths Reveal High-  
926 Grade Metamorphosed Forearc Complexes in NW China, v. 127, no. 6, p. e2022JB024309.

927 Wang, H. R., Zhao, H. G., Qiao, J. X., and Gao, S. H., 2013b, Theory and application of zircon U-Pb isotope dating  
928 technique: *Geology and Resources*, v. 22, no. 3, p. 229-232.

929 Wang, H. Y. C., Chen, H.-X., Zhang, Q. W. L., Shi, M.-Y., Yan, Q.-R., Hou, Q.-L., Zhang, Q., Kusky, T., and Wu, C.-M., 2017,  
930 Tectonic mélange records the Silurian–Devonian subduction-metamorphic process of the southern Dunhuang  
931 terrane, southernmost Central Asian Orogenic Belt: *Geology*, v. 45, no. 5, p. 427-430.

932 Wang, J. M., Lanari, P., Wu, F. Y., Zhang, J. J., Khanal, G. P., and Yang, L., 2021, First evidence of eclogites overprinted by  
933 ultrahigh temperature metamorphism in Everest East, Himalaya: Implications for collisional tectonics on early  
934 Earth: *Earth and Planetary Science Letters*, v. 558.

935 Wang, Q., 2020, Geochemical Characteristics and Geological Significance of Eclogite in Airikehansen Area, Dulan  
936 County, Qinghai Province: *Northwestern Geology*, v. 53, no. 1, p. 1-12.

937 Wang, Q., Zhao, J., Zhang, C., Yu, S., Ye, X., and Liu, X., 2022b, Paleozoic post-collisional magmatism and high-  
938 temperature granulite-facies metamorphism coupling with lithospheric delamination of the East Kunlun  
939 Orogenic Belt, NW China: *Geoscience Frontiers*, v. 13, no. 1, p. 101271.

940 White, R. W., Powell, R., Holland, T. J. B., Johnson, T. E., and Green, E. C. R., 2014, New mineral activity-composition  
941 relations for thermodynamic calculations in metapelitic systems: *Journal of Metamorphic Geology*, v. 32, no. 3,  
942 p. 261-286.

943 Whitney, D. L., and Evans, B. W., 2010, Abbreviations for names of rock-forming minerals: *American Mineralogist*, v. 95,  
944 no. 1, p. 185-187.

945 Wood, B. J., 1973, Garnet-orthopyroxene and orthopyroxene-clinopyroxene relationship in simple and complex  
946 systems: *Contributions to Mineralogy&Petrology*, v. 42, no. 2, p. 109-124.

947 Wu, C., Li, J., Zuza, A. V., Haproff, P. J., Chen, X., and Ding, L., 2021, Proterozoic– Phanerozoic tectonic evolution of the  
948 Qilian Shan and Eastern Kunlun Range, northern Tibet: *GSA Bulletin*.

949 Wu, C., Liu, C., Fan, S., Zuza, A. V., Ding, L., Liu, W., Ye, B., Yang, S., and Zhou, Z., 2020, Structural analysis and tectonic  
950 evolution of the western domain of the Eastern Kunlun Range, northwest Tibet: *GSA Bulletin*, v. 132, no. 5-6,  
951 p. 1291-1315.

952 Wu, C., Zuza, A. V., Chen, X., Ding, L., Levy, D. A., Liu, C., Liu, W., Jiang, T., and Stockli, D. F., 2019, Tectonics of the  
953 Eastern Kunlun Range: Cenozoic reactivation of a Paleozoic - early Mesozoic orogen: *Tectonics*, v. 38, no. 5, p.  
954 1609-1650.

955 Wu, Y., and Zheng, Y., 2004, Genesis of zircon and its constraints on interpretation of U-Pb age: *Chinese Science*  
956 *Bulletin*, v. 49, no. 15, p. 1554-1569.

957 Wu, Y. B., and Zhen, Y. F., 2004, Study on mineralogy of zircon formation and its constraints on U-Pb age interpretation:  
958 *Chinese Science Bulletin*, v. 49, no. 16, p. 1589-1604.

959 Xia, B., Cui, Y., Shang, Y. F., and Shi, J. T., 2022a, Petrology of Eclogite at Huwan, Western Dabie and Implications for  
960 Phase Equilibrium Modeling on LT-HP/UHP Eclogite: *Journal of Earth Science*. doi.org/10.1007/s12583-022-  
961 1719-9.

962 Xia, B., Shang, Y. F., Lu, X. B., and Wu, Y. B., 2022b, UHP eclogite from western Dabie records evidence of polycyclic  
963 burial during continental subduction: *American Mineralogist*. doi.org/10.2138/am-2022-8446

964 Xiao, W. J., Windley, B. F., Yong, Y., Yan, Z., Yuan, C., Liu, C. Z., and Li, J. L., 2009, Early Paleozoic to Devonian multiple-  
965 accretionary model for the Qilian Shan, NW China: *Journal of Asian Earth Sciences*, v. 35, no. 3-4, p. 323-333.

966 Xu, X., Song, S., and Su, L., 2016, Formation age and tectonic significance of the Wanbaogou basalts in the middle East  
967 Kunlun orogenic belt: *ACTA PETROLOGICA ET MINERALOGICA*, v. 35, no. 6, p. 16.

968 Yang, J. S., Jiang, C. F., Feng, B. G., Zhu, Z. Z., Zhao, M., Shi, X. D., and Hu, J. Q., 1986, An outline on the tectonics of the

969 Kunlun region: Bulletin of the Institute of Geology Chinese Academy of Geological Sciences, v. 2, p. 010.

970 Yang, J. S., Robinson, P. T., Jiang, C. F., and Xu, Z. Q., 1996, Ophiolites of the Kunlun Mountains, China and their tectonic  
971 implication: Tectonophysics, v. 258, no. 1-4, p. 215-231.

972 Yang, J. S., Wang, X. B., Shi, R. D., Xu, Z. Q., and Wu, C. L., 2004, The Dur'ngoi ophiolite in East Kunlun, northern  
973 Qinghai-Tibet Plateau: a fragment of paleoTethyan oceanic crust: Zhongguo Dizhi(Geology in China), v. 31, no.  
974 3, p. 225-239.

975 Yu, J., Zheng, Y., Xu, R., Hou, W., and Cai, P., 2020a, Zircon U-Pb Chronology, Geochemistry of Jiangjunmu Ore-Bearing  
976 Pluton, Eastern Part of East Kunlun and Their Geological Significance: Earth Science, v. 45, no. 4, p. 1151-1167.

977 Yu, M., Dick, J. M., Feng, C., Li, B., and Wang, H., 2020b, The tectonic evolution of the East Kunlun Orogen, northern  
978 Tibetan Plateau: A critical review with an integrated geodynamic model: Journal of Asian Earth Sciences, v.  
979 191, p. 104168.

980 Yu, S., Zhang, J., Li, H., Hou, K., Mattinson, C. G., and Gong, J., 2013a, Geochemistry, zircon U-Pb geochronology and Lu-  
981 Hf isotopic composition of eclogites and their host gneisses in the Dulan area, North Qaidam UHP terrane:  
982 New evidence for deep continental subduction: Gondwana Research, v. 23, no. 3, p. 901-919.

983 Yu, S., Zhang, J. X., Gong, J. H., and Li, Y. S., 2013b, Research on HP granulite-facies metamorphism and anatexis: A case  
984 study of Dulan area in the North Qaidam Mountains: Acta Petrologica Sinica, v. 29, no. 6, p. 2061-2072.

985 Zhang, G. B., Ellis, D. J., Christy, A. G., Zhang, L. F., and Song, S. G., 2010a, Zr-in-rutile thermometry in HP/UHP eclogites  
986 from Western China: Contributions to Mineralogy&Petrology, v. 160, no. 3, p. 427-439.

987 Zhang, G. B., Ireland, T., Zhang, L. F., Gao, Z., and Song, S. G., 2016, Zircon geochemistry of two contrasting types of  
988 eclogite: Implications for the tectonic evolution of the North Qaidam UHPM belt, northern Tibet: Gondwana  
989 Research, v. 35, p. 27-39.

990 Zhang, G. B., Niu, Y. L., Song, S. G., Zhang, L. F., Tian, Z. L., Christy, A., and Han, L., 2015a, Trace element behavior and P-

991 T-t evolution for partial melting of exhumed eclogite in the North Qaidam UHPM belt (NW China):  
992 implications for adakite genesis: *Lithos*, v. 226, p. 65–80.

993 Zhang, G. B., Zhang, L. F., and Song, S. G., 2012, An overview of the tectonic evolution of North Qaidam UHPM belt:  
994 From oceanic subduction to continental collision: *Geological Journal of China Universities*, v. 18, no. 1, p. 28-  
995 40.

996 Zhang, J. X., Mattinson, C. G., Meng, F. C., Wan, Y., and Tung, K., 2008, Polyphase tectonothermal history recorded in  
997 granulitized gneisses from the north Qaidam HP/UHP metamorphic terrane, western China: Evidence from  
998 zircon U-Pb geochronology: *Geological Society of America Bulletin*, v. 120, no. 5-6, p. 732-749.

999 Zhang, J. X., Meng, F. C., Li, J. P., and Mattinson, C. G., 2009, Coesite in eclogite from the North Qaidam Mountains and  
1000 its implications: *Chinese Science Bulletin*, no. 6, p. 1105-1110.

1001 Zhang, J. X., Meng, F. C., Wan, Y. S., Yang, J. S., and Dong, G. A., 2003, Early Paleozoic tectono-thermal event of the  
1002 Jinshuikou Group on the southern margin of Qaidam: Zircon U-Pb SHRIMP age evidence: *GEOLOGICAL*  
1003 *BULLETIN OF CHINA*, v. 22, no. 6, p. 397-404.

1004 Zhang, J. X., Yu, S. Y., Li, Y. S., Yu, X. X., Lin, Y. H., and Mao, X. H., 2015b, Subduction, accretion and closure of Proto-  
1005 Tethyan Ocean: Early Paleozoic accretion/collision orogeny in the Altun-Qilian-North Qaidam orogenic system:  
1006 *Acta Petrologica Sinica*, v. 31, no. 12, p. 3531-3554.

1007 Zhang, J. X., Yu, S. Y., and Mattinson, C. G., 2017, Early Paleozoic polyphase metamorphism in northern Tibet, China:  
1008 *Gondwana Research*, v. 41, p. 267-289.

1009 Zhang, Y. F., Pei, X. Z., Ding, S. P., Li, R. B., Feng, J. Y., Sun, Y., Li, C., and Chen, Y. X., 2010b, LA-ICP-MS zircon U-Pb age of  
1010 quartz diorite at the Kekesha area of Dulan County, eastern section of the East Kunlun orogenic belt, China  
1011 and its significance: *Geological Bulletin of China*, v. 29 no. 1, p. 79-85.

1012 Zhang, Y. L., Zhang, X. J., Hu, D. G., Shi, Y. R., and Lu, L., 2010c, SHRIMP zircon U-Pb ages of rhyolite from the Naj Tal



- 1013 group in the East Kunlun orogenic belt: *Journal of Geomechanics*, v. 16, no. 1, p. 21-27.
- 1014 Zhao, G. C., Wang, Y. J., Huang, B. C., Dong, Y. P., Li, S. Z., Zhang, G. W., and Yu, S., 2018, Geological reconstructions of  
1015 the East Asian blocks: From the breakup of Rodinia to the assembly of Pangea: *Earth-Science Reviews*, v. 186,  
1016 p. 262-286.
- 1017 Zheng, Y.-F., Zhang, L., McClelland, W. C., and Cuthbert, S., 2012, Processes in continental collision zones: Preface:  
1018 *Lithos*, v. 136-139, p. 1-9.
- 1019 Zhou, W., Xiaocheng, z., and Xinbiao, L., 2020, Petrology, Geochemistry and Chronology of the Baishahe Formation in  
1020 Numohong Area of Eastern Kunlun Orogenic Belt: *Journal of Earth Science*, v. 45, no. 12, p. 4370-4388.
- 1021 Zuza, A. V., Wu, C., Reith, R. C., Yin, A., Li, J., Zhang, J., Zhang, Y., Wu, L., and Liu, W., 2017, Tectonic evolution of the  
1022 Qilian Shan: An early Paleozoic orogen reactivated in the Cenozoic: *GSA Bulletin*, v. 130, no. 5-6, p. 881-925.
- 1023

1024 **Figure and Table captions**

1025 **Figure captions:**

1026 **Figure 1.** (A) The location of the northern part of Qinghai-Tibet Plateau. (B) Geological sketch map  
1027 of the East Kunlun Orogenic belt (modified after [Meng et al., 2017](#); [Zhang et al., 2015b](#);  
1028 [Zhang et al., 2017](#)) and the location of the eclogites in the Nuomuhong area and other  
1029 segments ([Meng et al., 2013b](#); [Qi et al., 2014](#); [Qi et al., 2016a](#); [Song et al., 2018b](#)). (C) The  
1030 approximately N-S structural cross-section of the Nuomuhong area showing main rock types  
1031 and the location of samples.

1032

1033 **Figure 2.** Field photographs of eclogite at Nuomuhong, in East Kunlun. (A) Eclogite block  
1034 enclosed in the host felsic gneiss. (B) Eclogite retrograded to amphibolite at edges. The red  
1035 dashed line marks the boundary between the retrograde eclogite and amphibolite. (C) The red  
1036 dashed line showing boundary between retrograde eclogite and the host felsic gneiss. (D)  
1037 Marble intercalated in amphibolite that showing banded structure. (E) The host felsic gneiss  
1038 consisted mainly of felsic minerals, biotite and garnet. (F) The retrograde eclogite consisted of  
1039 mainly garnet, clinopyroxene, amphibole and quartz.

1040

1041 **Figure 3.** Photomicrographs of representative eclogite at Nuomuhong, EKOB. Mineral  
1042 abbreviations are after [Whitney and Evans \(2010\)](#). (A) A large garnet porphyroblast from the  
1043 eclogite LH 3–5 showing apparent zoning with abundant inclusions in the reddish core and  
1044 minor in the light rim. Amphibole (Amp II), plagioclase, ilmenite and biotite (Bt) develop  
1045 around the garnet. (B) Backscattered electron image (BSE) of the garnet porphyroblast in Fig.

1046 3A showing inclusions of titanite (Ttn) and omphacite (Cpx I<sub>a</sub>) in the core. (C–D) Corona of  
1047 plagioclase (Pl III) + amphibole (Amp II) ± ilmenite (LH3–4) around a relict garnet  
1048 porphyroblast with inclusions of omphacite (Cpx I<sub>a</sub>). Symplectite of plagioclase (III) +  
1049 amphibole develops in the matrix; (E–F) Symplectite of orthopyroxene (Opx)+ plagioclase (Pl  
1050 II) around relict omphacite in matrix from the sample LH3–4. Corona of symplectite amp II +  
1051 Pl develops around relict garnet and low-sodic clinopyroxene (Cpx II<sub>a</sub>; light-colored in BSE)  
1052 develops around relict omphacite porphyroblast (Cpx I<sub>b</sub>; dark-colored in BSE). (G) Locally  
1053 enlarged BSE image in Fig. 3D showing transition from relict omphacite porphyroblast (Cpx I<sub>b</sub>;  
1054 with no Opx) to clinopyroxene porphyroblast (Cpx II<sub>b</sub>; with Opx), then to symplectite of Amp  
1055 II + Pl II; (with Opx). Corona of plagioclase (Pl III) + amphibole (Amp II) rims garnet; (H)  
1056 Rutile as inclusions in garnet or in matrix from the sample LH 3–2. It has been partial replaced  
1057 by ilmenite; (I) Amphibole (Amp I) included in garnet from sample LH 3–2. (G–K) Plane-  
1058 polarized photo with corresponding BSE image showing Biotite around amphibole (Amp II)  
1059 from sample LH 3–5.

1060

1061 **Figure 4.** Backscattered electron image of the garnet porphyroblast (LH 3–4) with EPMA  
1062 composition section (A, B) and the locally enlarged photo of inclusions (3) with the mineral  
1063 assemblage of Ep + Pl (Ab). (D) Diagram showing the compositional variation of garnet  
1064 porphyroblast, the Grt<sub>(mantle+core)</sub> (Grt I) and Grt<sub>trim</sub> (Grt II) are both group C-type after [Coleman  
1065 et al. \(1965\)](#). (E) Zoning profile of  $X_{alm} [=Fe^{2+}/(Fe^{2+} + Mn + Mg + Ca)$ ,  $X_{sps}$ ,  $X_{prp}$  and  $X_{grs}$   
1066 defined accordingly across garnet in the eclogite samples LH 3–4 from the Nuomuhong area].

1067

1068 **Figure 5.** Mineral chemistry diagrams. (A–B) Ternary classification diagrams for pyroxenes of the  
1069 Nuomuhong eclogites, after [Morimoto \(1988\)](#): (A) The classification diagram for Quad-Jd-Ae.  
1070 (B) The classification diagram for Wo-En-Fs. (C–D) The classification diagrams for  
1071 amphiboles of Nuomuhong eclogite, after [Leake et al. \(2004\)](#) and [Song et al. \(2018b\)](#). (E) Ab–  
1072 An–Or diagram showing the composition of plagioclase, after [Smith \(1974\)](#);  $Ab = X_{Na} = Na / (Ca$   
1073  $+ K + Na)$ ;  $An = X_{Ca} = Ca / (Ca + K + Na)$ ;  $Or = X_K = K / (Ca + K + Na)$ .

1074  
1075 **Figure 6.** Mineral assemblages for different metamorphic stages. Solid lines indicate minerals  
1076 present in the samples, whereas the dashed line refers to inferred minerals.

1077  
1078 **Figure 7.** Raman spectra of (A) omphacite (Omp) inclusions, (B) omphacite/jadeite inclusions, and  
1079 (C) garnet (Grt) and omphacite inclusions in zircon (Zrn) grains from the Nuomuhong  
1080 retrograde eclogite, middle East Kunlun orogen.

1081  
1082 **Figure 8.** Chondrite-normalized REE distribution patterns (A) and primitive mantle-normalized  
1083 spidergram of the retrograde eclogites and garnet amphibolites (B). The chondrite and  
1084 primitive mantle values are from [\(Sun and McDonough, 1989\)](#).

1085  
1086 **Figure 9.** (A–B) Zircon CL images, (C) SHRIMP U–Pb age concordia diagram and weighted mean  
1087  $^{206}\text{Pb}/^{238}\text{U}$  ages and (D) Chondrite-normalized REE distribution patterns for the Nuomuhong  
1088 retrograde eclogite LH3–4.

1089

1090 **Figure 10.** (A)  $P$ – $T$  pseudosection for Nuomuhong eclogite sample LH 3–4 (MnNCKFMASHTO  
1091 system); (B) Grossular  $[Ca/(Ca+Mg+Fe+Mn) *100]$  and pyrope  $[Mg/(Ca+Mg+Fe+Mn) *100]$   
1092 isopleths.

1093  
1094 **Figure 11.** Tectonic discrimination diagrams (A–D) for the retrograde eclogite (A) Zr–Zr/Y diagram  
1095 (Pearce and Norry, 1979); (B) Ce/Yb–Ta/Yb diagram (Pearce, 1982); (C) Y–La–Nb diagram  
1096 (Cabanis and Lecolle, 1989); (D) Nb–Zr–Y diagram (Meschede, 1986); (E) AFM diagram  
1097 (Irvine and Baragar, 1971). WPB–Within Plate Basalts; IAB–Island Arc Basalts; MORB–Mid-  
1098 Ocean Ridge Basalts.

1099  
1100 **Figure 12.** The  $P$ – $T$  path for the Nuomuhong eclogite in this study, in comparison with eclogite in the  
1101 eastern segment of the East Kunlun orogen from Song et al. (2018b). Boundaries for various  
1102 metamorphic facies, High- $P$  granulite, UHT follow Schreyer (1988), Syracuse et al. (2010) and  
1103 Maruyama et al. (1996), metamorphic facies, their abbreviations, and phase equilibria are after Liou et  
1104 al. (2004).

1105  
1106 **Figure 13.** Tectonic model for the Eastern Kunlun orogen, and Proto-Tethys Ocean.

1107

1108 **Table captions:**

1109 **Table S1.** Representative electron microprobe analyses of garnet in eclogite samples.

1110 **Table S2.** Representative analyses of clinopyroxene (omphacite) in eclogite samples.

1111 **Table S3.** Representative microprobe analyses of low-sodic clinopyroxene in eclogite samples.

1112 **Table S4.** Representative microprobe analyses of amphibole in eclogite samples.

1113 **Table S5.** Representative microprobe analyses of plagioclase in eclogite samples.

1114 **Table S6.** Representative microprobe analyses of other minerals (orthopyroxene and epidote) in

1115 eclogite samples

1116 **Table S7.** Whole rock major (wt%) and trace element (ppm) analyses of eclogites in Nuomuhong

1117 area, EKOB.

1118 **Table S8.** SHRIMP Zircon U-Pb isotopic data from the eclogite in Nuomuhong area, EKOB.

1119